Empirical constraints on extrusion mechanisms from the upper margin of an exhumed high-grade orogenic core, Sutlej valley, NW India

Empirical constraints on extrusion mechanisms from the upper margin of an exhumed high-grade orogenic core, Sutlej Valley, NW India

Jennifer Chambers*, Department of Earth and Environmental Sciences, CEPSAR, The Open University, Milton Keynes MK7 6AA, UK; Fax: +44 (0)1908 655151; e-mail: j.a.chambers@open.ac.uk

Mark Caddick, Institute for Mineralogy and Petrology, ETH Zürich, NW, Clausiusstrasse 25, CH 8092, Switzerland; Fax: +41 (0)44 632 16 36; e-mail: mark.caddick@erdw.ethz.ch

Tom Argles, Department of Earth and Environmental Sciences, CEPSAR, The Open University, Milton Keynes MK7 6AA, UK; Fax: +44 (0)1908 655151; e-mail: t.w.argles@open.ac.uk

Matthew Horstwood, NERC Isotope Geosciences Laboratory, Kingsley Dunham Centre, Keyworth, Nottingham NG12 5GG, UK; Fax: +44 (0)115 936 3302; email: msah@bgs.ac.uk

Sarah Sherlock, Department of Earth and Environmental Sciences, CEPSAR, The Open University, Milton Keynes MK7 6AA, UK; Fax: +44 (0)1908 655151; e-mail: s.sherlock@open.ac.uk

Nigel Harris, Department of Earth Sciences and Environmental Sciences, CEPSAR, The Open University, Milton Keynes MK7 6AA, UK; Fax: +44 (0)1908 655151; e-mail: n.b.w.harris@open.ac.uk

Randall Parrish, NERC Isotope Geosciences Laboratory, Kingsley Dunham Centre, Keyworth, Nottingham NG12 5GG, UK, *and* Department of Geology, University of Leicester, Leicester LE1 7RH, UK; Fax: +44 (0)115 936 3200; email: rrp@nigl.nerc.ac.uk

Talat Ahmad, Department of Geology, University of Delhi, Delhi-110007, India; Fax: +91 11 27666295; email: tahmad001@gmail.com

* Corresponding author

Abstract:

The Early–Middle Miocene exhumation of the crystalline core of the Himalaya is a relatively well-understood process compared to the preceding phase of burial and prograde metamorphism in the Eocene–Oligocene. Highly deformed rocks of the Greater Himalayan Sequence (GHS) dominate the crystalline core, and feature a strong metamorphic and structural overprint related to the younger exhumation. The Tethyan Sedimentary Series was tectonically separated from the underlying GHS during the Miocene by the South Tibetan Detachment, and records a protracted and complex history of Cenozoic deformation. Unfortunately these typically low-grade or unmetamorphosed rocks generally yield little quantitative pressure–temperature–time information to accompany this deformation history. In parts of the western Himalaya, however, the basal unit of the Tethyan Sedimentary Series (the Haimanta Group) includes pelites metamorphosed to amphibolite facies. This presents a unique opportunity to explore the tectono-thermal evolution of crystalline rocks which record the early history of the orogen.

Pressure–temperature–time–deformation (*P-T-t-d*) paths modelled for two Haimanta Group pelitic rocks reveal three distinct stages of metamorphism: (1) prograde Barrovian metamorphism to 610–620 °C at c. 7–8 kbars, with garnet growing over an early tectonic fabric (S_1); (2) initial decompression during heating to 640–660 °C at c. 6–7 kbars, with development of a pervasive crenulation cleavage (S_2) and staurolite and kyanite porphyroblast growth; (3) further exhumation during cooling, with minor retrograde metamorphism and modification of the pervasive S_2 fabric. Monazite growth ages constrain the timing of initial garnet growth (>34 Ma), the start of D_2 and maximum burial (c. 30 Ma), and the termination of garnet growth (c. 28 Ma). Muscovite Ar/Ar ages indicate cooling through c. 300 °C at c. 13 Ma, from which we derive an initial exhumation rate of c. 1.3 mm yr^{-1} for the Haimanta Group. The underlying GHS was exhumed at a rate of 2.2 to 3 mm yr^{-1} during this time. The difference in exhumation rate between these two units is considered to reflect Early Miocene displacement on the intervening South Tibetan Detachment. Slower exhumation (c. 0.6

mm yr^{-1}) of both units after c. 13 Ma followed the cessation of major displacement on this structure, after which time the Haimanta Group and the GHS were exhumed as one relatively coherent tectonic block.

Keywords: orogenesis; Himalaya; Haimanta Group; pseudosections; *P–T–t–d* paths, exhumation

1. Introduction

As an active zone of Cenozoic crustal deformation (e.g. Hodges, 2000; Aitchison et al., 2007), the Himalayan orogen is the focus of numerous studies examining the mechanical response to this process (Harris, 2007 and references therein). Critical to this challenge are tectonic reconstructions and models revealing how, when, and on what scale rocks were deformed, metamorphosed and transported within the evolving orogen. Pressure–temperature–time–deformation (*P–T–t–d*) data provide a record of the integrated effects of the thermal and mechanical processes involved, and present important constraints on model feasibility. Furthermore, identification of distinct tectono-stratigraphic units, e.g. the Greater Himalayan Sequence (GHS), and their bounding faults e.g. the Main Central Thrust (MCT), provides an invaluable framework for tectonic reconstructions. Here we present new *P–T–t–d* data from the uppermost tectono-stratigraphic unit of the crystalline core.

Gneisses and migmatites of the GHS (Le Fort, 1975; Yin, 2006) dominate the crystalline core of the Himalaya (Fig. 1). *P–T–t–d* data from the GHS have provided key constraints for mechanical models of the evolving Himalayan orogen (e.g. Beaumont et al., 2001; Jamieson et al., 2004). These data suggest that the GHS was overthrust, buried and metamorphosed during the Eocene–Oligocene ('M1' or 'Eohimalayan' phase), and then exhumed as the highly-deformed GHS during the Early–Middle Miocene ('M2' or 'Neohimalayan' phase) (Vance and Harris, 1999; Hodges, 2000; Vannay et al., 2004). Exhumation was facilitated by simultaneous reverse and normal sense motion on the MCT and South Tibetan Detachment (STD), respectively (Godin et al., 2006; Yin, 2006). Leucogranite intrusion into the GHS (the High Himalayan Leucogranites) records an approximately isothermal phase of decompression associated with this (Harris and Massey, 1994). In many cases, the younger 'Neohimalayan' phase has strongly overprinted metamorphic and structural records of the earlier history. A notable exception exists in the uppermost GHS of central Nepal (Vannay and Hodges, 1996; Coleman and Hodges, 1998; Gleeson and Godin, 2006), but generally the early tectono-thermal evolution of the crystalline

core is much less well-constrained than its Miocene exhumation (Hodges, 2000; Godin et al., 2001).

Studies on the major tectono-stratigraphic unit above the GHS, the Tethyan Sedimentary Series (TSS, Fig. 1) (Thakur, 1992) reveal a long and complex history of Tertiary deformation invaluable for understanding early orogenic processes (Ratschbacher et al., 1994; Wiesmayr and Grasemann, 2002; Godin, 2003). These rocks are typically unmetamorphosed or low-grade, with few well-developed U–Pb or Sm–Nd bearing metamorphic phases, so detailed structural studies cannot usually be coupled to *P–T* data and absolute ages. However, in parts of the western Himalaya, the base of the Phanerozoic TSS, the Haimanta Group, is metamorphosed up to amphibolite-grade. This unit has been correlated to the Phe Formation in Zanskar (Thakur, 1992), the Everest Series (also known as the North Col Formation) in eastern Nepal (e.g. Searle et al., 2003), the Upper Bhimphedi Group in the Kathmandu Nappe (Yin, 2006), and the Harsil Formation in Garhwal (Metcalfe, 1990; Prince, 1999). Due to the location of the Haimanta Group in the hanging wall of the STD, this unit is likely to retain valuable information regarding the early evolution of the Himalaya, owing to its tectonic separation from the underlying GHS during 'Neohimalayan' high-grade deformation.

This study uses petrographic, geochemical and geochronological (Ar/Ar mica and U–Pb monazite) data to record, date and model the high-grade metamorphism of the Haimanta Group in the Sutlej valley, NW India. We present the first comprehensive account of the *P–T–t–d* evolution of this unit, which constitutes the structurally highest crystalline rocks in the Himalayan core. These data help to constrain the Eocene to Oligocene development of the young Himalayan orogen, and contribute further to our understanding of the thermo-tectonic evolution of the crystalline core into and since the Miocene.

2. Geology of the upper Sutlej valley

Metasediments of the Haimanta Group (Hayden, 1904) consist of interlayered psammitic and pelitic schists with minor calcareous layers. The main foliation is a regular crenulation cleavage (Fig. 3a) with an associated ENE-plunging stretching lineation (Fig. 2c). The crenulation cleavage decreases in intensity up-section towards a low-grade spaced solution-cleavage (locality 18, Fig. 2a). Competent psammitic and calcareous beds define meso-scale folds (Fig. 3b), to which the main foliation is axial planar. On the macro-scale, a broad synform (axial plane inclined to the SW) strikes ~NW–SE across the upper Sutlej valley folding the dominant foliation (Fig. 2b, c).

The Lower Haimanta Group was intruded by the Ordovician (c. 488 Ma) Akpa (also termed 'Kinnaur Kailas') granite (Marquer et al., 2000; Miller et al., 2001). Pelites in close proximity to the granite show highly variable structures (Fig. 2c) probably reflecting strain heterogeneities in the 'shadow' of the granite during Himalayan deformation. In places, the margin of the granite itself has been deformed and has developed synkinematic kyanite, presumably during Tertiary orogenesis. The interior of the granite is relatively undeformed. Xenoliths of the Haimanta Group have been found within the granite (Vannay and Grasemann, 1998; Marquer et al., 2000). The sharp contact between the base of the Akpa granite (locally deformed to augengneiss) and migmatitic gneisses of the Vaikrita Group (Greater Himalayan Sequence) represents a ductile–brittle strand of the South Tibetan detachment (STD), locally termed the 'Sangla detachment'. Mylonites in this shear zone preserve evidence of both early SW-directed and later E-directed ductile shearing, as a result of the normal sense reactivation of a foreland-propagating thrust (Vannay et al., 2004). These ductile fabrics have been overprinted by a broad zone of steep brittle faults accommodating further E-directed extension (Vannay and Grasemann, 1998, and own authors' observations).

Metamorphic grade in the Haimanta Group decreases rapidly up-section; kyanite-staurolite-garnet mica schists are exposed at the structurally lowest level (adjacent to the Akpa granite) and are successively overlain by lower grade rocks up to greenschist facies

within a structural distance of approximately 6 km (Fig. 2a, b). Kyanite porphyroblasts near Morang (Fig. 2a) occur as large (average 4 cm long) blades restricted to certain compositional layers. A detailed metamorphic description of these high-grade rocks is presented in the following section. The uppermost (biotite) zone, midway between the Akpa granite and the Leo Pargil dome, preserves original sedimentary features including ripples and clay drapes.

Metamorphic grade increases systematically further NE, reaching kyanite grade near the Leo Pargil dome, which is comparable to the North Himalayan gneiss domes observed further east (Watts and Harris, 2005). The metasediments exposed within the Leo Pargil dome (Fig. 2) are indistinguishable in appearance from the Haimanta Group seen south of the Sutlej–Spiti confluence, with the exception of chaotically-orientated, mainly discordant leucogranite veins which increase in proportion towards the centre of the dome, where granite constitutes more than 50% of the exposures at Nako (Fig. 2a). The western edge of the dome is flanked by both ductile and brittle detachments, and although no detachment has yet been traced south across the Sutlej valley in the field, a continuation of the brittle detachment is inferred from satellite imagery (Thiede et al., 2006). Unmetamorphosed Tethyan sediments lie in the hanging wall of the detachment that exhumed the Leo Pargil dome (Thiede et al., 2006), and in sections to the west these clearly overlie the Haimanta Group on an unconformity (Wiesmayr and Grasemann, 2002).

3. Pressure-temperature-deformation (*P–T–d*) analysis

Petrographic examination of c. 100 thin sections from over 30 samples revealed two pelitic samples, 8i and 14i (see Fig. 2a for respective localities), that are representative of proposed *P–T–d* trends and are described in some detail below. Textural and chemical analyses were undertaken to relate growth and/or resorption of mineral phases to microstructures, and quantify major-phase compositions and zoning trends (Appendix A). Combined with whole-rock major element analyses (Table 1), these data allow us to model *P–T–d* evolution using the pseudosection approach (Powell et al., 1998).

3.1 Textural analysis

3.1.1 Sample 8i

An early tectonic fabric (S_1) consists of aligned plagioclase feldspar (euhedral to subhedral and with distinct zoning), biotite and minor white mica. A second fabric-forming event (D_2) led to the development of a crenulation cleavage (S_2) that is the dominant fabric of the Haimanta Group (Figs. 3a and 4). The deformation responsible for S_2 is likely to represent a stage of deformation in the continuum of crustal shortening, as opposed to a discrete deformation event associated with a distinct geological process. S_2 is defined by mats of fine-grained white mica aligned in parallel bands along the limbs of the crenulated S_1 fabric (Fig. 4a, c). S_1 biotite and white mica feature sweeping extinction and/or polygonal recrystallization as a result of deformation and/or recrystallization in crenulation hinges, whereas S_1 plagioclase (stronger than quartz and micas) is either fractured or internally altered (Fig. 4a). Quartz inclusion trails in subhedral garnet porphyroblasts (0.5–2 mm), and oblique to the external foliation (Fig. 4b, d), also represent S_1. Trails are either straight, or weakly sigmoidal suggesting synkinematic garnet growth over a weakly deformed S_1 fabric during the early stages of D_2. In places biotite grew mimetically upon plagioclase and garnet, from which we infer that biotite growth outlasted the growth of these other phases.

Porphyroblasts of staurolite (0.5–3 cm) and kyanite (1–3 mm) grew during a later stage of D_2, overprinting S_2 and occluding garnet (Fig. 4b–d). The final stage of deformation (D_3) tightened the S_2 crenulation cleavage about these porphyroblasts (including garnet where not occluded), modifying (but not completely transposing) S_2 to form 'S_2m' (Fig. 4c, d). Asymmetric pressure shadows around porphyroblasts suggest a component of simple shear (Fig. 4c). However, determining an unequivocal shear sense for this late deformation phase was not possible, because the geometry of the pressure shadows appears to have been modified by minor rotation of the porphyroblasts.

Staurolite continued to grow during D_3, overprinting a progressively modified S_2 fabric recorded by the change in orientation of inclusion trails in staurolite continuously towards the

tip, finally merging with 'S_2m' (Fig. 4b). However, D_3 outlasted staurolite growth, as shown by deformed white mica crystals wrapping around the end of staurolite porphyroblasts and featuring a sweeping extinction. Meanwhile, kyanite suffered internal deformation, and the crystal lattice is now either kinked (Fig. 4d), and/or degraded along crystal edges parallel to D_3 microfolds.

3.1.2 Sample 14i

Sample 14i shares a number of features with sample 8i: garnet porphyroblasts overgrew S_1 and grew up to early-D_2 (Fig. 5); staurolite porphyroblasts post-dated garnet growth (in places occluding garnet) and overprinted the main crenulation cleavage (S_2); D_3 modified S_2 into a tighter crenulation cleavage, forming pressure shadows around porphyroblasts which are asymmetric but lack an unambiguous sense of shear.

Garnet (2–5 mm) is the most abundant porphyroblast, with euhedral crystals preserved alongside more anhedral grains, including some which were evidently fractured. This sample contains no white mica and S_2 is defined by biotite laths (<0.5 mm) in a polygonally recrystallized plagioclase-rich matrix of anhedral grains with an average size of 50 μm. S_2 strongly wraps garnet porphyroblasts (Fig. 5). Staurolite porphyroblasts are relatively small (1–3 mm). Tightly folded and boudinaged mm-scale quartz veins preserve evidence of the S_2 crenulated cleavage, that has been eradicated and/or underdeveloped elsewhere. These quartz veins are also kinked about porphyroblasts, as a result of D_3 shearing/porphyroblast rotation.

3.1.3 Retrograde metamorphism

Minimal retrograde metamorphism is found in samples 8i and 14i, although minor chlorite alteration of garnet and staurolite rims (more pronounced in D_3-related pressure shadows) is seen. The edges of some staurolite porphyroblasts in sample 14i are retrogressed to biotite and quartz, and more rarely, completely replaced by chlorite. All retrograde phases are randomly aligned, indicating post-tectonic crystallization.

Several samples from nearby localities preserve evidence of more extensive retrograde metamorphism, characterized by a partial to complete replacement of garnet by chlorite, and often restricted to particular lithological layers. Thus retrograde metamorphism was probably controlled mainly by the localized presence of fluids, resulting in a variably-retrogressed Haimanta Group.

3.2 Chemical zoning

Garnet porphyroblasts in the Haimanta Group feature prograde zoning (i.e. 'bell-shaped' profiles) in the major elements Fe and Mg (Fig. 6a, b, Appendix A). These trends are reversed in the outer 50–100 μm of the analysed crystals, recording late-stage diffusional re-equilibration with the matrix. Similar prograde zoning in Y is also preserved, albeit only weakly in sample 14i cf. sample 8i (Fig. 6d, Appendix A)

Complex zoning trends are observed across profiles of plagioclase feldspar in sample 8i (Fig. 6c, Appendix A): anorthite content sharply decreases at the rim of the high-anorthite core, and either continues to decrease (although less significantly) or increases towards the edge of the crystal. Plagioclase in 14i is characterised by a more simple zoning profile, with low-anorthite cores increasing smoothly to anorthite-rich rims (Appendix A).

3.3 Modelled P–T–d evolution

The textural and chemical data above help to constrain detailed *P–T–d* paths through pseudosection diagrams, calculated for the bulk rock compositions of samples 8i and 14i (Table 1) with the mineral end-member data of Holland and Powell (1998). Free energy minimisations utilised the Perplex program of Connolly (1990), following the gridding scheme discussed by Connolly (2005). High compositional resolution was achieved following the adaptive pseudocompound generation method implemented in Perplex07 and outlined by Caddick and Thompson (2008). Solution models for complex phases were taken from Furhman and Lindsley (1988), Mahar et al. (1997), Holland et al. (1998), White et al. (2000), Powell and Holland (2001) and Coggon and Holland (2002) as detailed in Appendix I of

Caddick and Thompson (2008). Here we discuss the *P–T–d* histories implied by comparing the pseudosection predictions with the presence, absence and modal abundance of phases observed in samples 8i and 14i, and the measured chemical compositions of these phases

3.3.1 Sample 8i

An early stage of prograde metamorphism between 450 and 500 °C at 6 to 7 kbars is associated with an appreciable increase in the calculated proportion of biotite (Fig. 7b) and muscovite. Low-anorthite plagioclase is also stable at these *P–T* conditions and is consistent with analyzed plagioclase rims. The high-anorthite plagioclase cores, however, are only consistent with high-*T* (> 550 °C), low-*P* (1–4 kbars) conditions and are not easily reconciled with the moderate pressure history suggested by other phases (Fig. 7a). Therefore we suggest that the plagioclase cores are relicts of a pre-Himalayan (contact?) metamorphic event (e.g. Marquer et al., 2000; Gehrels et al., 2006).

Between c. 500 and 600 °C along the best-fit *P–T* path neither plagioclase nor rutile are predicted as stable phases. With *P* and *T* increase any pre-existing rutile is consumed by ilmenite forming reactions, compatible with the presence of ilmenite rather than rutile in this sample. Embayed plagioclase crystals suggest partial resorption of this phase, where slow dissolution rates at these temperatures presumably prohibitited its complete resportion. Garnet is predicted to be stable above 550 ˚C (Fig 7c), but analysed $X^{spessartine}$ and [Fe/Fe+Mg] ratios in garnet crystal cores (Fig. 6) coincide with calculated compositions at c. 575 °C (Figs 7d and 7e). Thus either garnet growth overstepped the calculated garnet-in reaction by c. 25 °C, as previously observed by Waters and Lovegrove (2002), or preserved crystal core compositions have been subsequently modified. Crystal rim compositions are consistent with garnet growth until c. 625 °C, although subsequent modification of rim compositions can also not be excluded. A calculated garnet proportion of approximately 4 % at 625 °C and c. 8 kbars agrees well with observed proportions. Pressure is less well-constrained than temperature for this part of the prograde path but textural evidence confirms the growth of garnet *then* staurolite, with this being most easily achieved at pressures above c. 6 kbars (Fig.

7a). Heating at lower pressure would result in garnet growth predominantly in staurolite-bearing assemblage fields.

A peak *T* of 660 °C at c. 7 kbars is constrained by the growth of ≤ 1% kyanite (Fig. 7a), with the best-fit *P–T* path experiencing decompression as this temperature is approached. Modal proportion isopleths imply additional minor garnet growth then weak resorption over this heating/decompression interval (Fig. 7c), although these details are probably lost in the thin, diffusionally-modified rims. The path through staurolite stability fields near peak *T* is consistent with petrographic observations that staurolite grew both pre and post kyanite growth. Plagioclase is also predicted as a stable phase throughout the high-temperature part of the modelled *P–T* path (Fig. 7a) but no plagioclase crystals with anorthite compositions calculated for this region were identified. This may partly reflect the sequestration of some Ca and Al into pre-existing high-anorthite plagioclase cores. As a D_2 crenulation began to form during the final stages of garnet growth, D_2 must have coincided with approximately peak pressure and the initial phase of exhumation accompanied by heating. The start of D_3 coincided with or closely followed peak *T* because both staurolite and kyanite overprint S_2 but only staurolite overprints S_2m.

The early part of the modelled retrograde path (decreasing *P* and *T*) is constrained to pressures above the sillimanite stability field as no sillimanite was observed in sample 8i, and staurolite is considered to have continued to grow during cooling to c. 640 ˚C. Abundant suitable nucleation substrates for sillimanite (e.g. biotite and white mica) in addition to matrix (D_3) deformation during this retrogressive phase suggests that the absence of observed sillimanite is a record of protracted stability above the kyanite–sillimanite transition, rather than inhibited sillimanite growth due to sluggish reaction rates.

3.3.2 Sample 14i

Sample 14i yields a similar best-fit *P–T–d* path (Fig. 8) to sample 8i described above, despite their strongly contrasting bulk-rock compositions (Table 1). In particular, sample 14i contains significantly more Fe, Mg, Ca and Na, and less Si and Al than 8i. Plagioclase

composition constrains the early part of the *P–T* history to pressures above 6 kbars, with calculated compositions at a lower *P* yielding significantly higher $X_{\text{plagioclase}}^{\text{anorthite}}$ than any analysed grains. Subsequent heating through the garnet-in reaction increases the calculated volume proportions of plagioclase and biotite towards c. 50 % and c. 35 %, respectively, consistent with petrographic observations.

$X_{\text{garnet}}^{\text{spessartine}}$ and $[\text{Fe/Fe+Mg}]_{\text{garnet}}$ contours for values representative of analysed crystal cores and rims constrain garnet growth to between 585 and 620 °C . As for sample 8i, an overstep of the garnet-in reaction of c. 25 °C is implied before initiation of garnet growth. Pressure is less well-constrained, but the grossular content of analysed crystals would be exceeded at pressures above c. 8 kbars. Peak *P* of the best-fit path (c. 7.5 kbars) coincides with a garnet volume proportion of 4 %, corresponding well with petrographic evidence. Furthermore, the absence of rutile indicates a maximum pressure of c. 7.5 kbars when peak *T* (c. 640 ˚C) is eventually reached.

A period of decompression accompanied by an increase in *T* to c. 640 °C is inferred as coeval with D_2. As peak *T* is approached staurolite growth is predicted. The modal proportions of both white mica and chlorite meanwhile decrease to 0 %, consistent with the notable absence of these prograde phases in this sample. These observations tightly constrain a peak *T* of c. 640 °C at c. 6–7 kbars (Fig. 8).

The absence of stable cordierite precludes isothermal decompression from peak *T* and the retrograde path is constrained to pressures above the cordierite-in reactions (Fig. 8). As D_3 post-dated staurolite formation in this sample, this deformation phase is restricted to the retrograde path.

3.3.3 Summary of P–T–d modelling results

The geometry of the two independently modelled *P–T–d* paths is strikingly similar, and is characterized by a distinctive three-phase evolution: (1) a moderate d*P*/d*T* prograde path to between 610 and 620 °C, 7–8 kbar; (2) an initial phase of c. 1 kbar decompression associated

with continued *T* increase to between 640 and 660 °C; (3) a retrograde path constrained by the lack of high-*T*, low-*P* minerals such as sillimanite or cordierite.

4 Geochronology

4.1 Monazite sampling and U–Pb methodology

Monazite ((Ce, La, Th) PO_4) grains are common throughout sample 14i, as is the case in other medium to high grade Himalayan metasediments (Martin et al., 2007). Their locations, in the matrix and in garnet porphyroblasts, presents a means of bracketing the age of garnet growth associated with prograde metamorphism. In turn, this can tightly constrain a segment of the *P–T–t* history.

Monazite grains from a number of thin sections of sample 14i were texturally characterized and chemically mapped using a Cameca SX100 electron microprobe. Both matrix monazites and monazite inclusions in garnet exhibit a similar shape (typically elongate and sub-rounded, but occasionally more rounded or anhedral), size (average 30 x 10 µm), and Y and Th contents (Y barely detectable and no hint of zoning; patchy Th zoning but consistently high-Th cores relative to rims, i.e. normally zoned, Fig. 9). Given that it was not possible to distinguish matrix monazite from included grains on morphological or chemical grounds, they were analysed *in-situ* (in thin section) using a laser ablation (LA) source to retain the textural context essential to our methodology. Monazite grains from three of the studied thin sections (including inclusions in six garnet porphyroblasts) were analysed. Grains exceeding 10 by 20 µm in size were considered analytically viable.

A UP193SS New Wave Research LA system was used in conjunction with a Nu multi-collector inductively coupled plasma mass spectrometer (MC–ICP–MS) instrument to ablate single spots (10 µm diameter) in monazite grains using laser fluences of 4–5 J cm^{-2}. Analysis followed methods similar to those described in Cottle et al. (2007) using the instrumental set-up modified from Simonetti et al. (2005). The 554 Ma Manangotry monazite was used as the reference for the Pb/U calibration, coupled with a static ablation pattern. The overall

reproducibility of the Manangotry standard for $^{206}Pb/^{238}U$ during the course of these analyses was 2 % (2σ), which has been propagated into the uncertainties for each spot analysis.

Considering that the sample grain sizes were barely larger than the LA spot size, it is expected that some analyses will have also sampled the surrounding phase; that is, garnet or biotite, and in one case, plagioclase feldspar. The U and ^{206}Pb concentrations of garnet were negligible; however those of biotite and feldspar could affect the data, and although great care was taken to avoid sampling these phases, data points for matrix monazites with an obvious common-Pb contribution indicative of a contaminated analysis were rejected. Inferred ages of monazite growth are based on U–Pb measurements, using Tera–Wasserburg concordia plots with projections through sample measurements onto the concordia from either a common-Pb composition or using linear arrays.

4.2 U–Pb monazite results (LA–MC–ICPMS)

The data have been carefully scrutinized and, despite very small grain sizes, young ages, and the consequent small signals for Pb isotopes (Table 2), are valid. All analyses of monazites occluded in garnet have Tera–Wasserburg age intercepts between c. 34 and 30 Ma, which may represent two crystallisation events: one at c. 34 Ma, represented by the data for four monazite grains from one garnet; the other event recorded by the majority of monazite inclusion analyses which define a colinear array of points yielding a lower intercept age of 29.61 ± 0.91 Ma and an upper intercept suggesting a Stacey and Kramers (1975) common-Pb composition equivalent to an age of c. 2588 Ma (Fig. 10a). The analysis that plots above and right of this linear array was not included in the regression as it is associated with relatively large errors which we infer to be the result of the impure nature of this particular grain (inclusions were identified and may not have been successfully avoided). Two analyses both with minor common-Pb and Tera–Wasserburg age intercepts between 32 and 33 Ma are inferred to have crystallized at c. 34 Ma and since suffered Pb-loss. Alternatively, these monazite grains plus others included in garnets from the same thin section (all with minor common-Pb) indicate a spread of $^{206}Pb/^{238}U$ ages from c. 34 to 30 Ma (Table 2, Fig. 10).

Two matrix grains also grew at c. 34–30 Ma (analyses plot in the dense cluster of data in Fig. 10b); one probably aged c. 34 Ma and the other c. 30 Ma, where each analysis includes a small component of common-Pb. However, the co-linearity of the majority of matrix monazite data suggests that a younger group of matrix grains formed at 27 ± 3 Ma. One discordant data point, plotting with a $^{206}Pb/^{238}U$ age of c. 26 Ma and with equivalent amounts of common-Pb to the other matrix grains, is interpreted simply to reflect the effect of Pb-loss from one of these monazites, the probable result of not being wholly occluded by its biotite host ("$m_{2a}1$", Fig. 5).

As with all monazite U–Pb data, excess ^{206}Pb tends to be a common occurrence. Unfortunately, the imprecision of ^{207}Pb–^{235}U ages (due to very low ^{207}Pb signals and lack of resolvable and correctable common-^{204}Pb) does not allow the extent of excess ^{206}Pb to be resolved, in contrast to the large ablation volume and high signal intensity data described by Horstwood et al. (2003) and Cottle et al. (2007). A compilation of the amount of excess of ^{206}Pb commonly present in monazite by Parrish (1990), suggests that the excess age attributable to excess ^{206}Pb in our samples is likely to lie in the range of 0.5–2.0 Myr. Thus, the age ranges quoted above represent maximum ages of growth, possibly overestimating by 0–2 Myr. Taking this into account we interpret that early monazite growth (predominantly grains occluded by garnet) and later (matrix) monazite growth took place in the periods 34–28 Ma and 30–22 Ma, respectively.

4.3 Ar/Ar mica sampling and methodology

Six samples of micaceous, greenschist to amphibolite facies metasediments were chosen for *in situ* Ar/Ar dating from a 25 km transect through the Haimanta Group. Sample selection aimed to provide a suite of unaltered schists ranging from close to the base of the Haimanta up to near the Cambro–Ordovician unconformity NW of Ropa village, representing a structural distance of approximately 6 km.

Micas in most samples crystallized during formation of the main (S_2) foliation, a crenulation cleavage, with the exception of those in sample 18. Bent, clear muscovite laths in this sample appear detrital, but the two muscovite analyses were performed on matrix domains of finely recrystallized white mica. Biotite in this sample was fine-grained and poorly developed, evidently at the lower limit of its metamorphic stability.

To determine the age of the samples, laser spots of approximately 50 µm in diameter were positioned in mica-rich domains using a focused CW Nd–Yag infrared laser with an external shutter. The samples were prepared by cutting 300 µm thick sections, polished on one side and ultrasonically cleaned alternately in methanol and de-ionised water. Pieces of thick section, approximately 5mm x 5mm in size, were wrapped in aluminium foil and irradiated at the McMaster Reactor (Canada) for 50 hours. The GA1550 biotite standard, with an age of 98.79 ± 0.96 Ma (Renne et al., 1998), was used to monitor the fast-neutron flux; the calculated J value is 0.01001 ± 0.0000501. The extracted argon isotopes ^{36}Ar to ^{40}Ar were measured in a MAP 215-50 noble gas mass spectrometer. Analyses were corrected for blanks measured either side of two consecutive samples analyses, ^{37}Ar decay and neutron-induced interference reactions using the correction factors: $(^{39}Ar/^{37}Ar)_{Ca}$ = 0.00065, $(^{36}Ar/^{37}Ar)_{Ca}$ = 0.000264 and $(^{40}Ar/^{39}Ar)_{K}$ = 0.0085, and the mass discrimination value used was 283.

4.4 Ar/Ar mica results

Ar/Ar ages (Table 3, Fig. 2a) are based on weighted averages of between 3 and 9 separate analyses as calculated using Isoplot 3 (Ludwig, 2003). Inverse isochron correlation diagrams have not been constructed due to the insufficient levels of ^{36}Ar in each measurement. The young age obtained from sample 20 (10.4 ± 2.3 Ma) most likely reflects the significantly finer grain size of the micas analyzed compared to other samples, as older ages would otherwise be expected from samples structurally higher in the section. Closure temperatures are lower for such fine-grained micas, which hence yield younger ages.

We note that although all Ar/Ar ages presented here are younger than those previously documented for both the Haimanta Group and underlying GHS, 19 – 17 Ma and 17 – 15 Ma,

respectively (Vannay et al., 2004), it is likely (especially for GHS samples) that the separated muscovite grains analyzed by those authors were coarser grained, and thus the older ages define an earlier point on the cooling path. The *in situ* muscovite ages and closure temperatures presented here correspond more closely to the zircon fission track data presented by Vannay et al. (2004).

We exclude biotite data from further calculations in the discussion because of the likely presence of excess ^{40}Ar. This common problem in metamorphic rocks (e.g. Sherlock and Kelley, 2002) is evident in our samples: for example, biotite and muscovite Ar/Ar ages for sample 23 are 14.5 Ma and 12.0 Ma, respectively, but closure temperature theory predicts that this relationship should be reversed (i.e. younger biotite than muscovite).

5. Discussion

Figure 11 provides a summary of the relative timing (and where possible, absolute ages) of metamorphism and deformation recorded in the Haimanta Group.

5.1 Timing of the modelled P–T–d path

The timing of monazite crystallization, derived from U–Pb monazite data (sample 14i), is assigned to the modelled prograde *P–T* path based on several lines of evidence: (1) simple Th zoning in monazite is consistent with fractionation during growth upon heating (Kohn and Malloy, 2004); (2) we found no textural evidence for the formation of retrograde monazite (e.g. after allanite; Bollinger and Janots, 2006); (3) smooth zoning profiles in garnet (Fig. 6) do not support the hypothesis that occluded monazite grains grew post-garnet growth along now annealed cracks; (4) retrograde metamorphism for this sample is minimal. Given that the garnet porphyroblasts preserve included phases from core to rim, and that monazite is restricted to the outer-core to rim regions (Fig. 5), monazite growth (beginning at c. 34 Ma) is interpreted to have post-dated the initiation of garnet growth. This explains the low Y content of the monazite grains, Y having been sequestered by earlier garnet growth (Pyle and Spear, 1999; Foster et al., 2002) as indicated by decreasing Y concentration from core to rim of

garnet crystals (Fig. 6d). If monazite grew as the result of a single reaction as implied by the simple Th zoning in the analyzed grains (Kohn and Malloy, 2004), we infer that the garnet-in reaction involving the breakdown of muscovite and chlorite released the necessary P and LREE to form monazite (Kohn and Malloy, 2004). The observed monazite-free garnet cores, however, suggest a delay between the first growth of garnet and the earliest recorded monazite grains. These observations imply monazite formation at ≥ 600 °C (taking into account an overstep of the garnet-in reaction, Figs. 7 and 8) rather than at lower *T* as a product of allanite breakdown (c. 350-400 °C; Wing et al., 2003). In contrast, monazite growth in the GHS of Garhwal grew both before and after garnet growth (Foster et al., 2000).

The ages of the youngest monazite grains occluded by garnet (c. 28 Ma) and of the analysed matrix grains (c. 27 Ma) bracket the final stage of garnet growth to c. 28 Ma. As the rims of garnet crystals record syn-tectonic growth during early-D_2, we infer that this phase of deformation began c. 30 Ma. Hence most matrix monazite grains, aged 27 ± 3 Ma, crystallized during D_2 with continued heating. Two older matrix grains (c. 34 and c. 30 Ma, Fig. 10b) are located in garnet pressure shadows, and we infer that these were protected from D_2 recrystallization. All other matrix monazite grains may have initially grown between 34 and 30 Ma and been subsequently recrystallized during D_2. Alternatively, matrix grains may merely preserve their various crystallisation ages (c. 34, 30 and 27 Ma), as the peak temperature for this sample (640 °C, Fig. 8) is significantly below the closure temperature for monazite (>800 °C, Spear and Parrish, 1996; Cherniak et al., 2004).

Garnet growth in the latest Eocene to Early Oligocene is consistent with data from elsewhere in the NW Himalaya, notably in the Harsil Formation, Garhwal (c. 36–30 Ma, Foster et al., 2000), but also in the underlying GHS of Garhwal (c. 36–30 Ma, Foster et al., 2000) and Zanskar (c. 33–28 Ma, Vance and Harris, 1999). A 35 ± 3 Ma kyanite-bearing leucosome in the uppermost GHS in central Nepal provides further evidence of high-grade Early Oligocene metamorphism (Godin et al., 1999).

The Oligocene high-grade metamorphism experienced by the Haimanta Group questions the suggestion that a pre-Tertiary event was responsible for the main deformation fabrics and metamorphic minerals (Marquer et al., 2000). Other than early plagioclase cores that we can only tentatively assign to a pre-Himalayan metamorphic event, we found no evidence for pre-Himalayan deformation and metamorphism including a striking lack of pre-Tertiary monazite (cf. Martin et al., 2007). This clearly does not preclude a pre-Tertiary metamorphic history for these samples, although it does imply a pervasive Oligocene overprint. Syn-kinematic kyanite observed in sheared Akpa granite at its upper contact with the Haimanta Group almost certainly formed during Tertiary metamorphism, and it is possible that deformation fabrics in xenoliths of the Haimanta Group also record Tertiary strain, especially where they are close to the granite margin.

5.2 Exhumation of the Haimanta Group

Following peak metamorphism, exhumation of the Haimanta Group was accompanied by cooling, in contrast to the isothermal decompression into sillimanite/cordierite then andalusite stability fields predicted by the channel flow model HT111 (Jamieson et al., 2006) for the *P–T* path 'D3' which corresponds to the position of the Haimanta Group. The model HT111 is considered representative of the field area as this model includes dome formation and could apply to the formation of the Leo Pargil dome. Earlier channel flow models (HT1, Jamieson et al., 2004) do not incorporate dome formation. This departure of *P–T–d* behaviour from the model predictions merits further investigation. In this section, we apply such constraints as are available, along with some approximations, to estimate segments of the exhumation history of parts of the Haimanta Group for comparison with other units.

Maximum depth of burial (c. 26–30 km for a lithostatic gradient of 3.7 km $kbar^{-1}$) occurred at c. 30 Ma, during the final stage of garnet growth (Figs. 6 and 7). An exhumation rate can be estimated for the interval between this point of maximum burial and the assumed depth at which an effective Ar diffusion closure temperature was reached for muscovite. Closure temperatures of 306 to 347 °C for cooling rates of 10 to 60 °C Myr^{-1}, corresponding

to the range of cooling rates calculated for the GHS and Haimanta Group (Vannay et al., 2004), were calculated using the Dodson equation (Dodson, 1973) and the diffusion parameters of Hames and Bowring (1994). For this range of closure *T*, extrapolation of the modelled retrograde path along a smooth curve of d*P*/d*T* yields a closure *P* of c. 2 kbars, equivalent to a depth of c. 7.4 km. This presents another inconsistency with *P–T* results from the channel flow model (HT111, Jamieson et al., 2006): at 12 Ma the model path 'D3' predicts *P–T* conditions of 6 kbars and 700 °C; in contrast, the Haimanta Group by this time had cooled to at least 347 °C at ~2 kbars. Thus the Haimanta Group was exhumed by c. 23 km during the interval from c. 30 Ma to c. 13 Ma, where 13 Ma is the average age of the weighted mean muscovite ages for samples 22 and 23 (sample 20 was excluded on the basis that its younger age with relatively high errors was probably a consequence of the very fine grain size and/or the small number of analyses). This is equivalent to a moderate exhumation rate of c. 1.3 mm yr^{-1}.

Exhumation and cooling of both the GHS and TSS (including the Haimanta Group) was controlled by thrusting along the MCT between c. 23 Ma and c. 16 Ma (Vannay et al., 2004). However, estimated rates of exhumation for the GHS in this period are between 2.2 mm yr^{-1} (Vannay et al., 2004) and c. 3 mm yr^{-1} (Caddick, 2004), notably higher than our estimation for the basal Haimanta Group of c. 1.3 mm yr^{-1}. This implies more efficient extrusion of the GHS between the MCT and the STD (Sangla detachment) than the rocks overlying the STD. In fact, c. 1 mm yr^{-1} is consistent with modern erosional rates for the southern edge of the Tibetan Plateau (Vance et al., 2003), and may represent a 'steady state' where exhumation is balanced by erosion, implying that by 23 Ma the Haimanta Group was essentially decoupled from the tectonically-extruding GHS beneath.

Calculations as described above yield lower average Haimanta Group exhumation rates of c. 0.6 mm yr^{-1} from c. 13 Ma to the present. GHS rocks also record a decrease in exhumation rate about the mid-Miocene (Vance et al., 2003; Vannay et al., 2004), suggesting that as the locus of thrusting propagated southwards into the Lesser Himalaya (Vannay et al.,

2004; Caddick et al., 2007; Chambers et al., 2008), both units were exhumed less rapidly and at similar rates of c. 0.6 mm yr^{-1}. From this we infer that following the cessation of GHS extrusion between the MCT and STD, both the Haimanta Group and the underlying GHS behaved as a more coherent block. Given that this re-coupling occurred at approximately the closure temperature of Ar in muscovite (c. 300 °C), the rocks were passing through the brittle–ductile transition for quartz–feldspar aggregates (Passchier and Trouw, 1996) and as a consequence ductile motion on the Sangla detachment between them was inhibited. Brittle structures are poorly developed along this segment of the STD, consistent with a lack of differential exhumation of the two units at high levels in the crust as suggested by these data.

The pervasive, gently-dipping, generally symmetrical crenulation cleavage in the Haimanta Group, as well as randomly-oriented kyanite crystals in the schists near sample 8, suggests that pure shear strain was dominant during initial exhumation. Evidence for ductile simple shear is very sparse in the Haimanta Group; kinematic indicators (e.g. garnet porphyroblast systems) were uncommon at most localities. Where present, opposing shear senses were recorded by approximately equal numbers of kinematic indicators, again implying dominantly pure shear. The preserved metamorphic field gradient between samples 8, a kyanite–staurolite–garnet–mica schist, and 18, a phyllite containing patchily developed biotite, is c. 43 °C km^{-1} (Table 4). Comparison with an estimated gradient of c. 20 °C km^{-1} between the same samples at their peak temperatures implies vertical thinning after peak metamorphism occurred in this section. The preserved field gradients calculated here cannot be equated with instantaneous geotherms, but the difference between these estimates is sufficient to demand explanation, especially because the samples occur in an apparently continuous, coherent section with consistent structures, and hence are unlikely to have experienced significant differential lateral displacement. Although the implied ductile vertical shortening (c. 47%) is not as extreme as examples reported from some other orogens (e.g. Argles et al., 1999), it provides important insights into the tectonic evolution of the STD hanging wall. We propose that the Haimanta Group experienced ductile vertical shortening,

dominantly by pure shear, during initial exhumation and S_2 fabric formation from c. 30 Ma until c. 23 Ma. Further exhumation of the underlying GHS between c. 23 Ma and c. 16 Ma was accomplished by ductile extrusion beneath the extensional Sangla detachment. This phase is represented in the hanging wall (Haimanta Group) by the development of simple shear ductile structures that modify S_2 (i.e. the D_3 stage), which may also have contributed to vertical thinning of the section. However, it is important to note that we did not observe any major brittle structures between localities 8 and 18 that could have excised substantial parts of the section, as was demonstrated in the Betic Cordillera by Argles et al. (1999). From this structural evolution we infer the age of peak *T* on the modelled *P–T–t–d* paths (Figs. 7 and 8), which is marked by the transition from D_2 to D_3 preserved in sample 8i, at c. 23 Ma (Fig. 1).

5.3 Tectonic implications of the Haimanta Group

Despite a relatively minor difference in metamorphic grade between the basal Haimanta Group (kyanite-grade) and the uppermost GHS (sillimanite-grade) seen in the Sutlej valley, there are several crucial reasons for separating them into two distinct tectonic units: (1) they are separated by a mylonite zone with both top-to-the-SW (thrust) and overprinting top-to-the-NE (normal) shear sense indicators that clearly define a major tectonic boundary; (2) they display different structural styles: a constantly oriented crenulation cleavage in the Haimanta Group, but a highly disrupted and deformed migmatitic foliation in the GHS gneisses; (3) the Haimanta Group lacks any evidence of *in situ* melt, which is abundant in the underlying rocks, both as deformed kyanite-bearing leucosomes and later segregations associated with sillimanite-grade metamorphism; (4) decoupled exhumation between c. 23 and 16 Ma resulted in distinct retrograde *P–T* paths, which for the GHS are characterised by decompression through muscovite-out reactions (Vance and Harris, 1999; Caddick, 2004; Harris et al., 2004).

The structures observed in the Haimanta Group (crenulation cleavage, flat-lying folds, weak to moderate stretching lineations) are incompatible with extreme ductile flow and thus preclude the assignment of this unit to a low-viscosity crustal channel (e.g. Beaumont et al.,

2001). The notable absence of *in situ* melt in the Haimanta Group supports this deduction, with *in situ* melting as identified in parts of the GHS providing a means of weakening leading to flow beneath southern Tibet (Zhang et al., 2004). Thus, the Haimanta Group may represent a relatively passive 'lid' to a 'GHS channel' localising intense ductile deformation below. Having been buried to greater depths than the Haimanta Group, and consequently attained higher temperatures, a sufficiently melt-weakened GHS now exposed in the Sutlej valley may have formed a south-directed plastic flow during the Late Oligocene–early Miocene, as proposed for rocks in central Nepal (Godin et al., 2007). The rheological contrast between the middle and upper crust (effectively the GHS and the Akpa granite/Haimanta Group, respectively) became such that they were decoupled during this phase of exhumation. Decompression before significant cooling in the GHS resulted in the 'Neohimalayan' phase of metamorphism, i.e. the high-T (sillimanite-grade) 'event' associated with melt generation, while the Haimanta Group was exhumed at more moderate rates associated with steady cooling. The lower peak temperatures attained in the Haimanta Group helped to preserve evidence of its 'Eohimalayan' burial history.

Ductile thinning of the Haimanta Group (lowermost TSS) during initial exhumation is consistent with predictions of the critical orogenic wedge model (Platt, 1986) for rocks near the rear of the wedge. However, this model assumes a uniform rheology for the wedge material (on a large scale), which is contrary to the weak mid-crustal layer, represented by the GHS, prescribed in the channel flow model (Beaumont et al., 2001). While vertical compression of the channel lid (i.e. the STD hanging wall) is not explicitly predicted by some channel flow numerical models (e.g. HT1, Jamieson et al., 2004), simulations involving a weakened upper crust do produce localised thinning of the channel lid and doming of the underlying high-grade material (model HT111, Jamieson et al., 2006). The thinned Haimanta section could be an expression of such crustal thinning above the nearby Leo Pargil dome, as is recognised in some crustal sections surrounding the North Himalayan Gneiss Domes

1 further east (Quigley et al., 2008). The Leo Pargil dome may thus represent the closest
2 channel doming to the STD currently recorded.

3 The Haimanta Group represents a distinct tectonic unit of the crystalline core of the
4 Himalaya. We recognise that it shares a strikingly similar tectonic evolution to that of the
5 uppermost GHS in central Nepal (Vannay and Hodges, 1996; Coleman and Hodges, 1998;
6 Godin et al., 2001; Gleeson and Godin, 2006), where the ductile Chame and brittle Phu
7 detachments are likely equivalent structures to the Sangla detachment and the detachment
8 north and east of the Leo Pargil dome (see Figure 1 in Thiede et al., 2006), respectively.
9 Gleeson and Godin (2006) propose that the uppermost GHS in central Nepal may be
10 equivalent to units up to 300 km further east along-strike, e.g. the Everest Series. Indeed, if
11 the Haimanta Group can be correlated with these units then it is of greater regional
12 significance than has been previously recognised.

13 **6. Conclusions**

14 Amphibolite facies metasediments of the Haimanta Group, seen in the western
15 Himalaya at the base of the Tethyan sediments and structurally above the GHS, record a
16 history of burial and heating to a maximum depth of <8 kbars at c. 600 °C. The ensuing phase
17 of decompression during further heating began at c. 30 Ma, and was accompanied by (D_2)
18 deformation resulting in the formation of a pervasive crenulation cleavage (S_2), and the
19 growth of staurolite and kyanite porphyroblasts. Continued cooling from a peak *T* of <660 °C
20 accompanied further decompression, and a temperature of 300–350 ˚C was reached at
21 approximately 2 kbars, by c. 13 Ma. The initial average exhumation rate of c. 1.3 mm yr^{-1}
22 during the interval c. 30 and 13 Ma was followed by a reduced average rate of c. 0.6 mm yr^{-1}
23 from 13 Ma to the present. During the first part of this exhumation history the underlying
24 GHS was more rapidly exhumed than the Haimanta Group, with the two units remaining
25 decoupled until c. 16 Ma. After c. 13 Ma, both units were exhumed at equal rates (c. 0.6 mm
26 yr^{-1}), implying exhumation as a single tectonic unit. The Haimanta Group is recognized as a

distinct tectono-thermal unit from the underlying GHS and, with along-strike correlatives, is important to reconcile with current models of Himalayan orogenesis.

Acknowledgements

Field work was supported by a NERC Research Studentship field grant (JC) and a NERC Research Grant NE/C513942/1 (TA and NH). MC was in receipt of ETH Research Funds. Analytical work at the NERC Isotope Geoscience Laboratory in the UK was supported by NIGF grant IP/868/1105. We thank Andy Tindle for his assistance with electron microprobe analyses, and to R. Jamieson, R. Law and an anonymous reviewer for their helpful reviews.

Appendix

Table of representative electron-microprobe analyses of zoned major minerals in samples 8i and 14i (Haimanta Group pelites) (Fig. 6).

References

Aitchison, J.C., Ali, J.R. and Davis, A.M., 2007. When and where did India and Asia collide? Journal of Geophysical Research-Solid Earth 112.

Argles, T.W., Platt, J.P. and Waters, D.J., 1999. Attenuation and Excision of a Crustal Section During Extensional Exhumation: The Carratraca Massif, Betic Cordillera, Southern Spain. Journal of the Geological Society, London 156, 149-162.

Beaumont, C., Jamieson, R.A., Nguyen, M.H. and Lee, B., 2001. Himalayan tectonics explained by extrusion of a low-viscosity crustal channel coupled to focused surface denudation. Nature 414, 738-742.

Bollinger, L. and Janots, E., 2006. Evidence for Mio-Pliocene retrograde monazite in the Lesser Himalaya, far western Nepal. European Journal of Mineralogy 18, 289–297.

Caddick, M., 2004. The Tectonometamorphic Evolution of the Central and Western Himalaya. PhD Thesis, Cambridge University.

Caddick, M.J., Bickle, M.J., Harris, N.B.W., Holland, T.J.B., Horstwood, M.S.A. and Ahmad, T., 2007. Burial and exhumation history of a Lesser Himalayan schist: Recording the formation of an inverted metamorphic sequence in NW India. Earth and Planetary Science Letters, 264, 375-390.

Caddick, M.J. and Thompson, A.B., 2008. Quantifying the tectono-metamorphic evolution of pelitic rocks from a wide range of tectonic settings: Mineral compositions in equilibrium. Contributions to Mineralogy and Petrology DOI 10.1007/s00410-008-0280-6.

Chambers, J.A., Argles, T., Horstwood, M., Harris, N., Parrish, R. and Ahmad, T., 2008. Tectonic implications of Palaeoproterozoic anatexis and Late Miocene metamorphism in the Lesser Himalayan Sequence, Sutlej Valley, NW India. Journal of the Geological Society, London 165, 725-737.

Cherniak, D.J., Watson, E.B., Grove, M. and Harrison, T.M., 2004. Pb diffusion in monazite: A combined RBS/SIMS study. Geochimica Et Cosmochimica Acta 68, 829-840.

Coggon, R. and Holland, T.J.B., 2002. Mixing properties of phengitic micas and revised garnet-phengite thermobarometers. Journal of Metamorphic Geology 20, 683-696.

Coleman, M.E. and Hodges, K.V., 1998. Contrasting Oligocene and Miocene thermal histories from the hanging wall and footwall of the South Tibetan detachment in the central Himalaya from Ar-40/Ar-39 thermochronology, Marsyandi Valley, central Nepal. Tectonics 17, 726-740.

Connolly, J.A.D., 1990. Multivariable phase diagrams: an algorithm based on generalized thermodynamics. American Journal of Science 290, 666-718.

Connolly, J.A.D., 2005. Computation of phase equilibria by linear programming: A tool for geodynamic modeling and its application to subduction zone decarbonation. Earth and Planetary Science Letters 236, 524-541.

Cottle, J.M., Jessup, M.J., Newell, D.L., Searle, M.P., Law, R.D. and Horstwood, M.S.A., 2007. Structural insights into the early stages of exhumation along an orogen-scale detachment: The South Tibetan Detachment System, Dzakaa Chu section, Eastern Himalaya. Journal of Structural Geology 29, 1781-1797.

Dodson, M.H., 1973. Closure temperature in cooling geochronological and petrological systems. Contributions to Mineralogy and Petrology 40, 259-274.

Ferry, J.M., 1984. A Biotite Isograd in South-Central Maine, U.S.A.: Mineral Reactions, Fluid Transfer, and Heat Transfer. Journal of Petrology 25, 871-893.

Foster, G., Gibson, H.D., Parrish, R., Horstwood, M., Fraser, J. and Tindle, A., 2002. Textural, chemical and isotopic insights into the nature and behaviour of metamorphic monazite. Chemical Geology 191, 183-207.

Fuhrman, M.L. and Lindsley, D.H., 1988. Ternary feldspar modeling and thermometry. American Journal of Science 73, 201-215.

1 Gleeson, T.P. and Godin, L., 2006. The Chako antiform: A folded segment of the Greater Himalayan
2 sequence, Nar Valley, Central Nepal Himalaya. Journal of Asian Earth Sciences 27, 717-734.

3 Godin, L., 2003. Structural evolution of the Tethyan sedimentary sequence in the Annapurna area,
4 central Nepal Himalaya. Journal of Asian Earth Sciences 22, 307-+.

5 Godin, L., Brown, R.L., Hanmer, S. and Parrish, R., 1999. Back folds in the core of the Himalayan
6 orogen: An alternative interpretation. Geology 27, 151-154.

7 Godin, L., Grujic, D., Law, R.D. and Searle, M.P., 2006. Channel flow, extrusion, and exhumation in
8 continental collision zones: an introduction. In: R.D. Law, M.P. Searle and L. Godin (Editors),
9 Channel Flow, Ductile Extrusion and Exhumation in Continental Collision Zones. Geological
10 Society, London, Special Publications, pp. 1-23.

11 Godin, L., Kellet, D. and Larson, K.P., 2007. Orogenic superstructure behaviour and mid-crustal plastic
12 flow in the central Nepal Himalaya. Eos Transactions, AGU 88(52), Fall Meeting Supplement,
13 Abstract T31D-0672.

14 Godin, L., Parrish, R.R., Brown, R.L. and Hodges, K.V., 2001. Crustal thickening leading to
15 exhumation of the Himalayan Metamorphic core of central Nepal: Insight from U-Pb
16 Geochronology and Ar-40/Ar-39 Thermochronology. Tectonics 20, 729-747.

17 Hames, W.E. and Bowring, S.A., 1994. An empirical evaluation of the argon diffusion geometry in
18 muscovite. Earth and Planetary Science Letters 124, 161-167.

19 Harris, N., 2007. Channel flow and the Himalayan-Tibetan orogen - a critical review. Journal of the
20 Geological Society 164, 511-523.

21 Harris, N. and Massey, J., 1994. Decompression and Anatexis of Himalayan Metapelites. Tectonics 13,
22 1537-1546.

23 Harris, N.B.W., Caddick, M., Kosler, J., Goswami, S., Vance, D. and Tindle, A.G., 2004. The pressure-
24 temperature-time path of migmatites from the Sikkim Himalaya. Journal of Metamorphic
25 Geology 22, 249-264.

26 Hayden, H.H., 1904. The Geology of the Spiti with parts of the Bashur and Rupshu. Geological Survey
27 of India 36, 121.

28 Hodges, K.V., 2000. Tectonics of the Himalaya and southern Tibet from two perspectives. Geological
29 Society of America Bulletin 112, 324-350.

30 Holland, T.J.B., Baker, J.M. and Powell, R., 1998. Mixing properties and activity-composition
31 relationships of chlorites in the system MgO-FeO-Al_2O_3-SiO_2-H_2O. European Journal of
32 Mineralogy 10, 395-406.

33 Holland, T.J.B. and Powell, R., 1998. An internally consistent thermodynamic data set for phases of
34 petrological interest. Journal of Metamorphic Geology 16, 309-343.

35 Gehrels, G.E., DeCelles, P.G., Ojha, T.P. and Upreti, B.N., 2006. Geologic and U-Pb geochronologic
36 evidence for early Paleozoic tectonism in the Dadeldhura thrust sheet, far-west Nepal
37 Himalaya. Journal of Asian Earth Sciences 28, 385-408.

38 Jamieson, R.A., Beaumont, C., Medvedev, S. and Nguyen, M.H., 2004. Crustal channel flows: 2.
39 Numerical models with implications for metamorphism in the Himalayan-Tibetan orogen.
40 Journal of Geophysical Research-Solid Earth 109, doi:10.1029/2003JB002811.

41 Jamieson, R.A., Beaumont, C., Nguyen, M.H. and Grujic, D., 2006. Provenance of the Greater
42 Himalayan Sequence and associated rocks: predictions of channel flow models. In: R.D. Law,
43 M.P. Searle and L. Godin (Editors), Channel Flow, Ductile Extrusion and Exhumation in
44 Continental Collision Zones. Geological Society, London, Special Publications, 165-182.

45 Kohn, M.J. and Malloy, M.A., 2004. Formation of monazite via prograde metamorphic reactions
46 among common silicates: implications for age determinations. Geochimica et Cosmochimica
47 Acta 68, 101-113.

48 Le Fort, P., 1975. Himalayas - Collided Range - Present Knowledge of Continental Arc. American
49 Journal of Science A275, 1-44.

Ludwig, K.R., 2003. Users manual for Isoplot/Ex version 3.0: a geochronological toolkit for Microsoft Excel. Berkeley Geochronology Center Spec. Pub. No. 4, Berkeley, California, 70 pp.

Mahar, E.M., Baker, J.M., Powell, R., Holland, T.J.B. and Howell, N., 1997. The effect of Mn on mineral stability in metapelites. Journal of Metamorphic Geology 15, 223-238.

Marquer, D., Chawla, H.S. and Challandes, N., 2000. Pre-alpine high-grade metamorphism in High Himalaya crystalline sequences: Evidence from Lower Palaeozoic Kinnaur Kailas granite and surrounding rocks in the Sutlej Valley (Himachal Pradesh, India). Eclogae Geologicae Helvetiae 93, 207-220.

Martin, A.J., Gehrels, G.E. and DeCelles, P., 2007. The tectonic significance of (U, Th)/Pb ages of monazite inclusions in garnet from the Himalaya of central Nepal. Chemical Geology 244, 1-24.

Metcalfe, R.P., 1990. A thermotectonic evolution for the Main Central Thrust and Higher Himalaya, Western Garhwal, India, University of Leicester.

Miller, C., Thöni, M., Frank, W., Grasemann, B., Klötzli, U., Guntli, P. and Draganits, E., 2001. The early Palaeozoic magmatic event in the Northwest Himalaya, India: source, tectonic setting and age of emplacement. Geological Magazine 138, 237-251.

Parrish, R.R., 1990. U-Pb dating of monazite and its application to geological problems. Canadian Journal of Earth Sciences 27, 1431-1450.

Passchier, C.W. and Trouw, R.A.J., 1996. Microtectonics. Springer, Berlin-Heidelberg-New York, 289 pp.

Platt, J.P., 1986. Dynamics of orogenic wedges and the uplift of high-pressure metamorphic rocks. Geological Society of America Bulletin 97, 1037-1053.

Powell, R., Holland, T. and Worley, B., 1998. Calculating phase diagrams involving solid solutions via non- linear equations, with examples using THERMOCALC. Journal of Metamorphic Geology 16, 577-588.

Powell, R. and Holland, T.J.B., 2001. Course Notes for "THERMOCALC Workshop 2001: Calculating Metamorphic Phase Equilibria" (on CD-ROM).

Prince, C.I., 1999. The timing of prograde metamorphism in the Garhwal Himalaya, India, The Open University, Milton Keynes.

Pyle, J.M. and Spear, F.S., 1999. Yttrium zoning in garnet: Coupling of major and accessory phases during metamorphic reactions. Geological Materials Research 1, 2-49.

Quigley, M., Liangjun, Y., Gregory, C., Corvino, A., Sandiford, M., Wilson, C.J.L. and Xiaohan, L., 2008. U–Pb SHRIMP zircon geochronology and *T–t–d* history of the Kampa Dome, southern Tibet. Tectonophysics 446, 97-113.

Ratschbacher, L., Frisch, W., Liu, G. and Chen, C., 1994. Distributed deformation in southern and western Tibet during and after the Indian-Asia collision. Journal of Geophysical Research 99(B10), 19917-19945.

Renne, P.R., Swisher, C.C., Deino, A.L., Karner, D.B., Owens, T.O. and DePaolo, D.J., 1998. Intercalibration of standards, absolute ages and uncertainties in $^{40}Ar/^{39}Ar$ dating. Chemical Geology 145, 117-152.

Searle, M.P., Simpson, R.L., Law, R.D., Parrish, R.R. and Waters, D.J., 2003. The structural geometry, metamorphic and magmatic evolution of the Everest massif, High Himalaya of Nepal-South Tibet. Journal of the Geological Society 160, 345-366.

Searle, M.P., Law, R.D. and Jessup, M.J., 2006. Crustal structure, restoration and evolution of the Greater Himalaya in Nepal - South Tibet: implications for channel flow and the ductile extrusion of the middle crust. In: R.D. Law, M.P. Searle and L. Godin (Editors), Channel Flow, Ductile Extrusion and Exhumation in Continental Collision Zones. Geological Society, London, Special Publications, pp. 355-378.

Sherlock, S.C. and Kelley, S.P., 2002. Excess argon in HP-LT rocks: a UV laserprobe study of phengite and K-free minerals. Chemical Geology 182, 619-636.

Simonetti, A., Heaman, L.M., Hartlaub, R.P., Creaser, R.A., MacHattie, T.G. and Bohm, C., 2005. U-Pb zircon dating by laser ablation-MC-ICP-MS using a new multiple ion counting Faraday collector array. Journal of Analytical Atomic Spectrometry 20, 677-686.

Spear, F.S. and Parrish, R.R., 1996. Petrology and Cooling Rates of the Valhalla Complex, British Columbia, Canada. Journal of Petrology 37, 733-765.

Stacey, J.S. and Kramers, J.D., 1975. Approximation of Terrestrial Lead Isotope Evolution by a 2-Stage Model. Earth and Planetary Science Letters 26, 207-221.

Thakur, V.C., 1992. Geology of Western Himalaya. Physics and Chemistry of the Earth, 19. Pergamon Press, Oxford-New York, 366 pp.

Thiede, R.C., Bookhagen, B., Arrowsmith, J.R., Sobel, E.R. and Strecker, M.R., 2004. Climatic control on rapid exhumation along the Southern Himalayan Front. Earth and Planetary Science Letters 222, 791-806.

Thiede, R.C., Arrowsmith, J.R., Bookhagen, B., McWilliams, M., Sobel, E.R. and Strecker, M.R., 2006. Dome formation and extension in the Tethyan Himalaya, Leo Pargil, northwest India. Geological Society of America Bulletin 118, 635-650.

Vance, D., Bickle, M., Ivy-Ochs, S. and Kubik, P.W., 2003. Erosion and exhumation in the Himalaya from cosmogenic isotope inventories of river sediments. Earth and Planetary Science Letters 206, 273-288.

Vance, D. and Harris, N., 1999. Timing of prograde metamorphism in the Zanskar Himalaya. Geology 27, 395-398.

Vannay, J.-C. and Grasemann, B., 1998. Inverted metamorphism in the High Himalaya of Himachal Pradesh (NW India): phase equilibria versus thermobarometry. Schweizerische Mineralogische Und Petrographische Mitteilungen 78, 107-132.

Vannay, J.-C., Grasemann, B., Rahn, M., Frank, W., Carter, A., Baudraz, V. and Cosca, M., 2004. Miocene to Holocene exhumation of metamorphic crustal wedges in the NW Himalaya: Evidence for tectonic extrusion coupled to fluvial erosion. Tectonics 23, TC1014.

Vannay, J.-C. and Hodges, K.V., 1996. Tectonomorphic evolution of the Himalayan metamorphic core between the Annapurna and Dhaulagiri, central Nepal. Journal of Metamorphic Geology 14, 635–656.

Waters, D.J. and Lovegrove, D.P., 2002. Assessing the extent of disequilibrium and overstepping of prograde metamorphic reactions in metapelites from the Bushveld aureole. Journal of Metamorphic Geology 20, 135-149.

Watts, D.R. and Harris, N.B.W., 2005. Mapping granite and gneiss in domes along the North Himalayan antiform with ASTER SWIR band ratios. Geological Society of America Bulletin 117, 879-886.

White, R.W., Powell, R., Holland, T.J.B. and Worley, B.A., 2000. The effect of TiO_2 and Fe_2O_3 on metapelitic assemblages at greenschist and amphibolite facies conditions: mineral equilibria calculations in the system K_2O-FeO-MgO-Al_2O_3-SiO_2-H2O-TiO_2-Fe_2O_3. Journal of Metamorphic Geology 18, 497-511.

Wiesmayr, G. and Grasemann, B., 2002. Eohimalayan fold and thrust belt: Implications for the geodynamic evolution of the NW-Himalaya (India). Tectonics 21.

Wing, B.A., Ferry, J.M. and Harrison, T.M., 2003. Prograde destruction and formation of monazite and allanite during contact and regional metamorphism of pelites: petrology and geochronology. Contributions to Mineralogy and Petrology 145, 228-250.

Yin, A., 2006. Cenozoic tectonic evolution of the Himalayan orogen as constrained by along-strike variation of structural geometry, exhumation history, and foreland sedimentation. Earth-Science Reviews 76, 1-131.

Zhang, H.F., Harris, N., Parrish, R., Kelley, S., Zhang, L., Rogers, N., Argles, T. and King, J., 2004. Causes and consequences of protracted melting of the mid-crust exposed in the North Himalayan antiform. Earth and Planetary Science Letters 228, 195-212.

Fig. 1. Generalized geological map of the Himalaya.

Fig. 2. (a) Geological sketch map of the upper Sutlej Valley, after Marquer et al. (2000; 2002), Wiesmayr and Grasemann (2002), Thiede et al. (2006) with modifications from the authors' field observations. Includes metamorphic isograds: bt, biotite; gt, garnet; st, staurolite; ky, kyanite; crd, cordierite (where the zone, as opposed to the 'mineral-in' line, is labelled). Ar/Ar ages are shown for samples from localities marked by open squares (bt, biotite; mu, muscovite). Grey triangles mark localities sampled for *P–T–t–d* analysis. Line A–A' marks the location of the cross-section in (b). (b) Cross-section with detailed foliation trajectories from field measurements, and metamorphic isograds, projected onto the line of section A–A' shown in (a). (c) Simplified and cropped geological sketch map showing stretching lineations from field measurements. Ornamentation for the Haimanta Group omitted for clarity. STD, South Tibetan detachment; GHS, Greater Himalayan Sequence; TSS, Tethyan Sedimentary Sequence.

Fig. 3. Outcrop photographs at locality 8 (Fig. 2a) of (a) the dominant fabric in the Haimanta Group pelites, a crenulation cleavage (S_2). Garnet porphyroblasts have been wrapped by this foliation (see bulge top centre, and indentation where garnet has fallen out, bottom right). Coin 2.5 cm; (b) Near flat-lying meso-scale fold (hinge line dips 3° towards SSE) depicted by competent psammitic and calcareous layers. Pelites contain an axial planar cleavage.

Fig. 4. Microphotographs of pelites from locality 8: (a) Sample 8i. S_1 plagioclase feldspar in S_2 crenulation cleavage is both fractured and altered (fractures rimmed by red-orange alteration product and/or dusty-looking internal alteration). Quartz is clear with low relief; laths of biotite and muscovite are dark and light grey respectively; (b) Sample 8i (b2 is a line-drawing of b1). Syn-tectonic garnet porphyroblast with faintly sinusoidal inclusion trails (S_1 weakly deformed by D_2) occluded by a large staurolite porphyroblast. Staurolite overprints S_2 (quartz inclusion trails oblique to S_1 in garnet), and towards its tip overprints a modified (by

D_3) S_2 fabric (also see (c)). D_3 out-lasts staurolite growth and fine laths of S_2 muscovite are wrapped around the tip of staurolite; (c) to show context of (b). S_2 (inclusion trails in staurolite) have been subsequently modified (S_2m) by D_3, tightening the S_2 crenulation cleavage and wrapping large porphyroblasts. Asymmetric pressure shadows suggests a component of simple shear and/or rotation of staurolite during D_3; (d) Sample 8ii. Cross polarised light. A garnet porphyroblast with S_1 inclusion trails is occluded by a kinked kyanite porphyroblast, with S_2 inclusion trails oblique to S_1. Post-kyanite growth, S_2 has been micro-folded against the porphyroblast during D_3.

Fig. 5. Back-scatter electron images of two garnet porphyroblasts from sample 14i, plus a selection of the monazite grains analysed (including one Mg-element map, of monazite "m_{4a}6"). Garnets overprint a pre-existing S_1 fabric, as well as an S_1–S_2 fabric at the rim consistent with late stage garnet growth syn-tectonic with early D_2. S_2, defined by the biotite/plagioclase matrix (light and dark grey matrix phases respectively), is oblique to S_1 and wraps garnet porphyroblasts. Chlorite (mid-grey between biotite and plagioclase) is present in the pressure shadows to garnet 4a (top and bottom of the image). Monazites are labelled with a prefix 'g' (garnet) or 'm' (matrix) which refers to the host phase, a subscript which refers to the section name (e.g. '2') and the occluding or adjacent garnet (e.g. 'a'), and a suffix which indicates the analysis number (Table 2). Where elongate, monazite grains are aligned with the tectonic fabric (e.g. "m_{2a}1", "m_{4a}6"). Some other grains are distinctly anhedral (e.g. "g_{2a}1" and "m_{2a}3"). Black scale bar (garnet images) 2 mm; white scale bar (monazite grain images), 100 µm.

Fig. 6. Chemical zoning in porphyroblasts (data provided in Appendix A): (a) and (b) major element variation across garnets from samples 8i and 14i respectively; (c) anorthite variation across plagioclase feldspars from both samples 8i and 14i, plotted so that their cores are aligned, 'pl' and 'perp' refer to parallel and perpendicular (respectively) to the length of the

crystal; (d) Y variation across garnets from both samples 8i and 14i, plotted so that their cores are aligned.

Fig. 7. (a) Pseudosection diagram for sample 8i, quartz and water also stable in every field. Best fit *P–T–d* path (including D_1, D_2 and D_3) shown. Abbreviated phases are garnet (Gt), staurolite (St), biotite (Bt), chlorite (Chl), muscovite (Mu), paragonite (Par), ilmenite (Ilm), rutile (Ru), plagioclase (Pl), titanite (Sph), albite (Ab), kyanite (Ky), sillimanite (Sil), andalusite (And), cordierite (Crd) and K-feldpsar (K-fsp). Al_2SiO_5 phase transitions are shown with solid lines in Al_2SiO_5-bearing fields and are extended into Al_2SiO_5-absent fields with dashed lines. Small assemblage fields unlabelled for clarity. Melt was not considered. Subplots (b) and (c) show calculated abundance of biotite and garnet, respectively. Subplots (d) and (e) show calculated garnet composition, $X_{\text{garnet}}^{\text{spessartine}}$ and Fe/Fe+Mg ratio, respectively. All subplots are at the same scale (have equivalent axes) to the main plot. Supplementary subplots are provided online.

Fig. 8. Pseudosection diagram for sample 14i, quartz and water also stable in every field. Best fit *P–T–d* path (including D_1, D_2 and D_3) shown. Abbreviated phases as in Figure 7 plus zoisite (Zoi). Al_2SiO_5 phase transitions are shown with solid lines in Al_2SiO_5-bearing fields and are extended into Al_2SiO_5-absent fields with dashed lines. Small assemblage fields unlabelled for clarity. Melt was not considered. Supplementary subplots are provided online.

Fig. 9. Th and Y maps of three representative monazite grains in sample 14i. Grains are normally zoned with respect to Th, whereas the concentration of Y is extremely low or beyond the levels of detection. See figure 5 for corresponding BSE images. Scale bar 50 µm.

Fig. 10. U–Pb monazite data from sample 14i. (a) Monazite inclusions in garnet porphyroblasts: black ellipses used in regression to a c. 30 Ma U–Pb age; bold grey ellipses

(of inclusions in the same garnet crystal) indicate a U–Pb age of c. 34 Ma; dashed black ellipses are inferred to represent c. 34 Ma monazites with a component of Pb loss; dashed grey ellipse omitted from regression owing to relatively large errors. (b) All data: grey ellipses represent all analyses shown in a); the regression is through all analyses of matrix monazite grains bar 3. See text for more details. Data point error ellipses are 2σ.

Fig. 11. Summary of the relative timing of metamorphism and deformation recorded in the Haimanta Group. Abbreviated mineral phases as in Figure 7.

Table 1. Whole-rock major element data (in weight %) for two high-grade Haimanta Group metapelites.

Table 2. U–Pb isotopic data of monazite grains in a garnet–mica schist (Haimanta Group sample 14i).

Table 3. Infrared laserprobe Ar/Ar age data. All measurements are in volts; the calculated ages include the error on J and are 2σ.

Table 4. Calculations of metamorphic field gradients in the Haimanta Group.

Table 1

Whole-rock major element data (in weight %) for two high-grade Haimanta Group metapelites

	SiO_2	TiO_2	Al_2O_3	Fe_2O_3	MnO	MgO	CaO	Na_2O	K_2O	P_2O_5	LOI	Total
8i	56.79	0.89	21.07	8.40	0.10	3.82	0.42	1.28	5.43	0.21	1.60	100.01
14i	53.25	0.83	19.10	9.54	0.11	6.13	1.59	4.44	3.67	0.18	0.44	99.29
"typical" pelite*	59.80		16.57	5.81	0.10	2.62	1.09	1.73	3.53			91.25

* from Mahar et al. (1997)

LOI, loss on ignition

Table 2

U-Pb isotopic data of monazite grains in a garnet-mica schist (Haimanta Group sample 14i)

Analysis	^{204}Pb	^{206}Pb	^{207}Pb	^{238}U	Pb	U	Uncorrected isotopic ratios							Uncorrected ages (Ma)					
	(cps)	(mV)	(mV)	(mV)	(ppm) †	(ppm) †	$^{207}Pb/^{206}Pb$	1σ (%)	$^{238}U/^{206}Pb$	1σ (%)	$^{207}Pb/^{235}U$	1σ (%)	Rho	$^{207}Pb/^{206}Pb$	2σ abs	$^{206}Pb/^{238}U$	2σ abs	$^{207}Pb/^{235}U$	2σ abs
Monazite in garnet																			
O.13	33	0.2	0.01	62	16	1319	0.0613	6.7	214	1.59	0.0396	6.9	0.23	651	287	30.1	1.0	39	5
O.15*	3	0.3	0.02	82	57	1752	0.0621	4.6	196	0.97	0.0437	4.7	0.20	676	198	32.9	0.6	43	4
O.16	120	0.3	0.02	81	46	1730	0.0642	4.5	193	0.97	0.0459	4.6	0.21	748	189	33.3	0.6	46	4
O.17	116	0.5	0.02	140	27	3003	0.0511	3.6	204	0.96	0.0346	3.7	0.26	247	165	31.5	0.6	35	3
2a.1*	-51	0.4	0.02	125	42	2675	0.0533	3.9	204	0.91	0.0360	4.0	0.23	344	178	31.5	0.6	36	3
2a.2	-69	0.3	0.02	92	84	1974	0.0596	4.3	192	1.35	0.0427	4.5	0.30	587	187	33.4	0.9	42	4
2a.4*	67	0.2	0.01	67	94	1424	0.0583	6.3	201	0.90	0.0399	6.3	0.14	539	274	32.0	0.6	40	5
2a.5*	104	0.3	0.02	90	56	1931	0.0579	4.7	202	0.94	0.0395	4.8	0.20	527	206	31.8	0.6	39	4
2a.6	-20	0.3	0.02	91	99	1944	0.0620	4.2	188	0.95	0.0456	4.3	0.22	676	178	34.2	0.6	45	4
2b.7*	54	0.3	0.01	83	33	1777	0.0568	5.1	199	0.96	0.0393	5.2	0.18	482	227	32.3	0.6	39	4
2b.10*	-26	0.5	0.02	139	20	2979	0.0511	3.7	207	1.09	0.0341	3.8	0.28	243	170	31.1	0.7	34	3
4a.1*	-32	0.2	0.01	63	21	1515	0.0540	6.3	187	1.08	0.0397	6.4	0.17	371	282	34.3	0.6	40	5
4a.3*	-152	0.3	0.01	75	20	1788	0.0526	5.5	187	1.22	0.0388	5.6	0.22	310	251	34.4	0.7	39	4
4a.10*	-162	0.4	0.02	101	114	2244	0.0546	4.3	187	1.02	0.0402	4.4	0.23	395	191	34.3	0.5	40	3
4a.11*	31	0.3	0.01	78	72	1735	0.0556	5.7	210	1.07	0.0366	5.8	0.18	437	255	30.7	0.5	36	4
4a.14*	-97	0.4	0.02	94	64	2074	0.0529	4.7	186	1.02	0.0391	4.8	0.21	324	211	34.5	0.5	39	4
4b.17	-13	0.2	0.01	66	54	1461	0.0540	6.7	200	1.03	0.0372	6.8	0.15	372	302	32.1	0.5	37	5
4c.19	20	0.4	0.02	103	157	2283	0.0516	4.5	196	1.05	0.0363	4.6	0.23	267	206	32.8	0.5	36	3
4c.21	3	0.3	0.01	92	23	2031	0.0505	5.7	215	1.24	0.0323	5.8	0.21	217	264	29.9	0.6	32	4
Matrix monazite																			
2a.1*	67	0.3	0.02	120	93	2562	0.0694	3.8	249	0.91	0.0384	3.9	0.23	911	158	25.8	0.5	38	3
2a.3*	-8	0.4	0.04	101	28	2150	0.1062	3.0	187	1.00	0.0783	3.2	0.31	1736	111	34.4	0.7	77	5
2a.4*	160	0.4	0.02	115	110	2454	0.0568	3.9	201	1.02	0.0389	4.0	0.25	482	171	31.9	0.6	39	3
2b.9	102	0.2	0.02	65	50	1393	0.0932	4.1	198	0.99	0.0650	4.2	0.24	1491	154	32.5	0.6	64	5
2b.11	32	0.3	0.02	89	57	1900	0.0806	7.5	209	1.64	0.0532	7.6	0.21	1211	294	30.8	1.0	53	8
2b.12	251	0.5	0.03	122	24	2599	0.0805	4.9	192	1.02	0.0579	5.0	0.21	1209	192	33.5	0.7	57	6
4a.4*	-304	0.3	0.02	84	119	2012	0.0560	4.7	182	1.03	0.0425	4.8	0.22	454	207	35.3	0.6	42	4
4a.5*	-41	0.3	0.02	79	40	1895	0.0811	4.0	196	1.03	0.0569	4.1	0.25	1223	157	32.8	0.5	56	4
4a.6*	-62	0.2	0.02	65	188	1447	0.0945	4.2	190	1.06	0.0687	4.3	0.25	1518	157	33.9	0.7	67	6
4a.7	200	0.3	0.02	75	193	1672	0.0841	4.5	211	1.14	0.0551	4.6	0.25	1295	174	30.5	0.7	54	5
4a.8	70	0.3	0.02	92	89	2050	0.0673	4.5	219	1.12	0.0423	4.6	0.24	847	187	29.3	0.5	42	4

* See Figure 5

† c. 20 % uncertainty on concentration

Table 3

Infrared laserprobe Ar/Ar age data. All measurements are in volts, the calculated ages include the error on J and are 2σ

Sample-Mineral	^{40}Ar	±	^{39}Ar	±	^{38}Ar	±	^{37}Ar	±	^{36}Ar	±	$^{40}Ar^*/^{39}Ar$	±	Age (Ma)	+/-
20-Wm	1.1618	0.0110	0.9917	0.0047	0.0125	0.0004	1.3427	0.0074	0.0021	0.0004	0.5577	0.1053	10.0	1.9
20-Wm	2.1705	0.0024	0.4868	0.0010	0.0082	0.0001	0.3855	0.0001	0.0064	0.0001	0.5859	0.0860	10.6	1.5
20-Wm	0.2096	0.0005	0.2173	0.0004	0.0024	0.0001	0.1177	0.0000	0.0003	0.0002	0.6108	0.2859	11.0	5.1
21-Bt	0.3481	0.0014	0.3488	0.0019	0.0043	0.0001	0.0029	0.0001	0.0002	0.0001	0.7948	0.0849	14.3	1.5
21-Bt	0.1623	0.0005	0.1404	0.0007	0.0017	0.0000	0.0005	0.0000	0.0001	0.0000	0.9138	0.0120	16.4	0.2
21-Bt	0.1843	0.0005	0.1605	0.0006	0.0021	0.0000	0.0010	0.0000	0.0002	0.0000	0.8075	0.0102	14.5	0.2
21-Bt	0.3641	0.0010	0.3868	0.0025	0.0032	0.0002	0.0147	0.0007	0.0002	0.0001	0.8076	0.0431	14.5	0.8
21-Bt	0.4121	0.0013	0.3555	0.0013	0.0039	0.0002	0.0083	0.0007	0.0006	0.0001	0.6314	0.0467	11.4	0.8
21-Bt	0.1643	0.0003	0.1354	0.0003	0.0015	0.0000	0.0062	0.0003	0.0002	0.0000	0.8867	0.0691	15.9	1.2
22-Wm	0.3344	0.0003	0.3478	0.0015	0.0040	0.0000	0.0005	0.0000	0.0003	0.0001	0.7150	0.0602	12.9	1.1
22a-Wm	0.2531	0.0004	0.2343	0.0010	0.0029	0.0001	0.0010	0.0000	0.0002	0.0000	0.8407	0.0183	15.1	0.3
22a-Wm	0.2137	0.0007	0.2031	0.0006	0.0023	0.0000	0.0005	0.0000	0.0002	0.0000	0.7464	0.0210	13.4	0.4
22a-Wm	0.3242	0.0006	0.3426	0.0002	0.0033	0.0001	0.0014	0.0001	0.0002	0.0000	0.7522	0.0216	13.5	0.4
22a-Wm	0.2218	0.0009	0.2102	0.0010	0.0025	0.0001	0.0012	0.0001	0.0002	0.0000	0.7921	0.0619	14.2	1.1
22a-Wm	0.2104	0.0008	0.2239	0.0015	0.0027	0.0000	0.0009	0.0001	0.0001	0.0000	0.7588	0.0582	13.6	1.0
22a-Wm	0.4092	0.0033	0.3922	0.0010	0.0046	0.0001	0.0010	0.0001	0.0002	0.0001	0.8797	0.0403	15.8	0.7
22a-Wm	0.1978	0.0003	0.1863	0.0002	0.0021	0.0000	0.0005	0.0001	0.0002	0.0000	0.8238	0.0502	14.8	0.9
22a-Wm	0.2615	0.0003	0.2602	0.0012	0.0033	0.0001	0.0004	0.0000	0.0001	0.0001	0.8745	0.0973	15.7	1.7
23-Bt	2.8174	0.0054	1.1911	0.0033	0.0157	0.0002	0.0020	0.0001	0.0063	0.0000	0.8098	0.0117	14.6	0.2
23-Bt	0.3705	0.0006	0.1527	0.0006	0.0021	0.0000	0.0001	0.0001	0.0008	0.0000	0.8588	0.0614	15.4	1.1
23-Bt	0.2776	0.0017	0.1655	0.0009	0.0020	0.0001	-0.0001	0.0004	0.0005	0.0000	0.8118	0.0340	14.6	0.6
23-Bt	0.7917	0.0010	0.3438	0.0015	0.0042	0.0000	0.0002	0.0001	0.0018	0.0000	0.7928	0.0369	14.2	0.7
23-Bt	1.0926	0.0013	0.4885	0.0016	0.0043	0.0002	0.0006	0.0001	0.0023	0.0000	0.8592	0.0288	15.4	0.5
23-Bt	1.0469	0.0013	0.5364	0.0014	0.0065	0.0000	0.0008	0.0001	0.0022	0.0000	0.7524	0.0261	13.5	0.5
23-Wm	0.7105	0.0015	0.4702	0.0022	0.0059	0.0001	0.0008	0.0001	0.0014	0.0000	0.6186	0.0203	11.1	0.4
23-Wm	0.2957	0.0006	0.2478	0.0015	0.0026	0.0001	0.0024	0.0003	0.0005	0.0000	0.6446	0.0380	11.6	0.7
23-Wm	0.2336	0.0011	0.1719	0.0013	0.0012	0.0001	0.0034	0.0007	0.0004	0.0000	0.7487	0.0364	13.5	0.7
23-Wm	0.4360	0.0009	0.3878	0.0027	0.0047	0.0002	0.0007	0.0001	0.0007	0.0000	0.6059	0.0246	10.9	0.4
23-Wm	0.8057	0.0014	0.4508	0.0003	0.0055	0.0001	0.0006	0.0001	0.0016	0.0000	0.7186	0.0239	12.9	0.4
23-Wm	0.5825	0.0007	0.4759	0.0003	0.0058	0.0001	0.0014	0.0001	0.0010	0.0000	0.6340	0.0224	11.4	0.4
23-Wm	0.6531	0.0015	0.4474	0.0010	0.0057	0.0000	0.0011	0.0001	0.0011	0.0000	0.7332	0.0212	13.2	0.4
23-Wm	0.2334	0.0005	0.2535	0.0010	0.0023	0.0001	0.0014	0.0003	0.0001	0.0001	0.7983	0.0998	14.4	1.8
23-Wm	0.2726	0.0004	0.2470	0.0010	0.0031	0.0001	0.0027	0.0001	0.0004	0.0000	0.6670	0.0324	12.0	0.6
23-Wm	0.3008	0.0007	0.2801	0.0011	0.0034	0.0001	0.0071	0.0005	0.0004	0.0000	0.6941	0.0336	12.5	0.6
Average blank	0.0096	0.0016	0.0005	0.0001	0.0005	0.0002	0.0003	0.0007	0.0012	0.0006				

Table 4
Calculations of metamorphic field gradients in the Haimanta Group

Sample/ section	Peak *T* (º C)	Peak *P* (kbar)[1]	Peak depth (km)[2]	Present distance (km)	Peak gradient (º C km^{-1})[3]	Present gradient (º C km^{-1})[3]	Vertical shortening factor
18	400	3.54	13	-	31	-	-
8	660	7	26	-	25	-	-
18 to 8	260	3.5	13	~6[5]	20	43	~2

[1] *P* at peak *T* conditions
[2] Calculated assuming lithostatic gradient of 3.7 km/kbar
[3] Metamorphic field gradient, not necessarily instantaneous geothermal gradient
[4] Estimated for biotite isograd (Ferry, 1984)
[5] Structural distance between samples 18 and 8 (Fig. 2a)

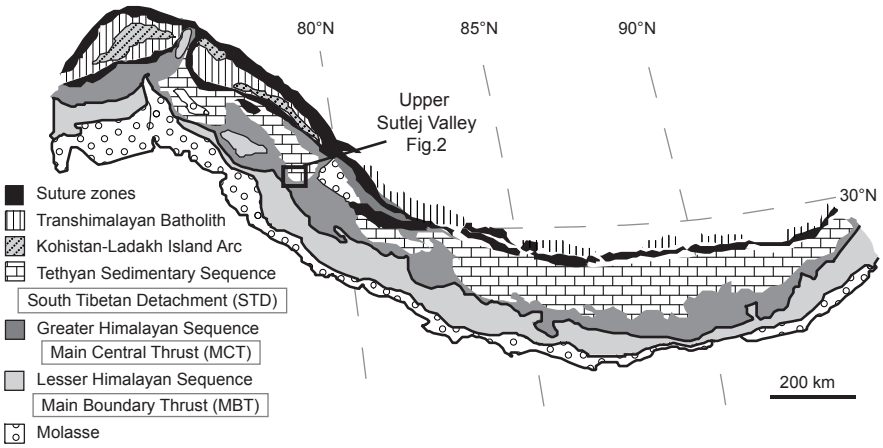

Fig. 1. Generalized geological map of the Himalaya.

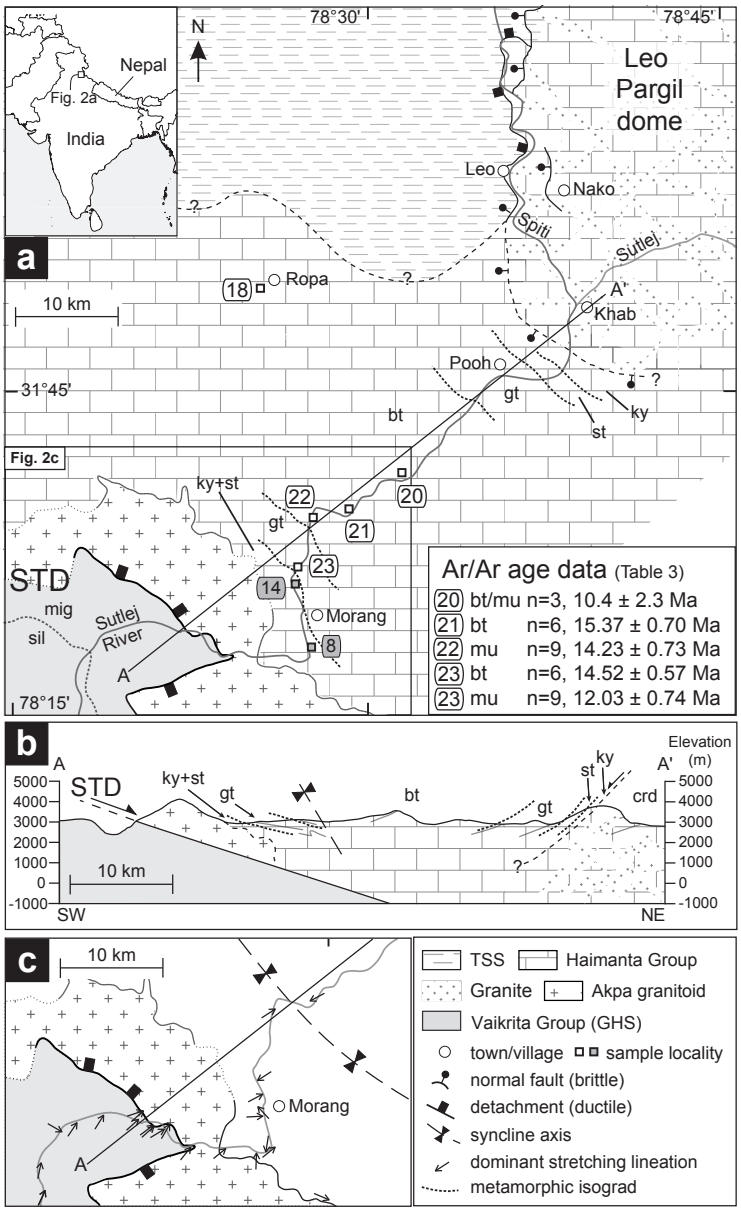

Fig. 2. (a) Geological sketch map of the upper Sutlej Valley, after Marquer et al. (2000; 2002), Wiesmayr and Grasemann (2002), Thiede et al. (2006) with modifications from the authors' field observations. Includes metamorphic isograds: bt, biotite; gt, garnet; st, staurolite; ky, kyanite; crd, cordierite (where the zone, as opposed to the 'mineral-in' line, is labelled). Ar/Ar ages are shown for samples from localities marked by open squares (bt, biotite; mu, muscovite). Grey triangles mark localities sampled for *P–T–t–d* analysis. Line A–A' marks the location of the cross-section in (b). (b) Cross-section with detailed foliation trajectories from field measurements, and metamorphic isograds, projected onto the line of section A–A' shown in (a). (c) Simplified and cropped geological sketch map showing stretching lineations from field measurements. Ornamentation for the Haimanta Group omitted for clarity. STD, South Tibetan detachment; GHS, Greater Himalayan Sequence; TSS, Tethyan Sedimentary Sequence.

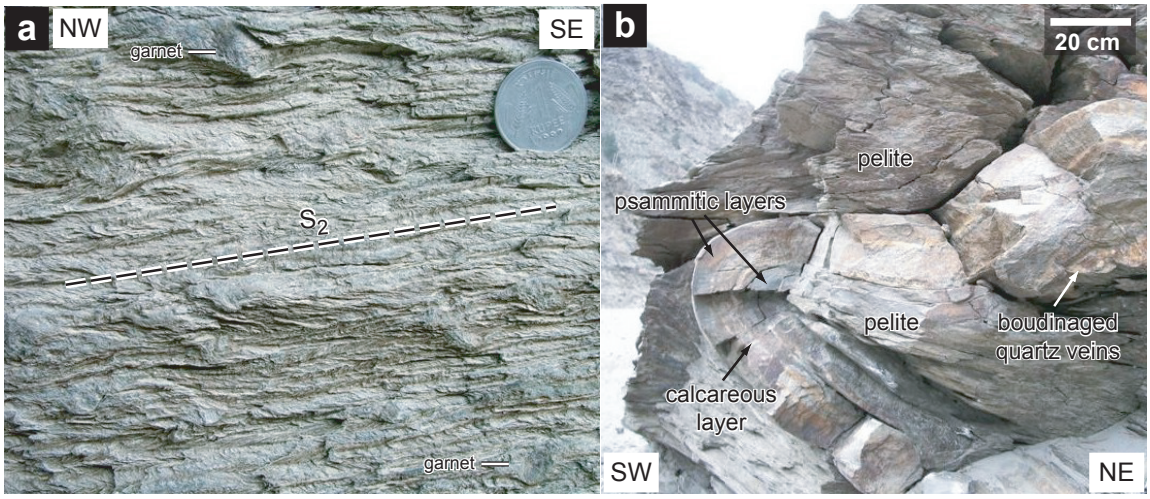

Fig. 3. Outcrop photographs at locality 8 (Fig. 2a) of (a) the dominant fabric in the Haimanta Group pelites, a crenulation cleavage (S_2). Garnet porphyroblasts have been wrapped by this foliation (see bulge top centre, and indentation where garnet has fallen out, bottom right). Coin 2.5 cm; (b) Near flat-lying meso-scale fold (hinge line dips 3° towards SSE) depicted by competent psammitic and calcareous layers. Pelites contain an axial planar cleavage.

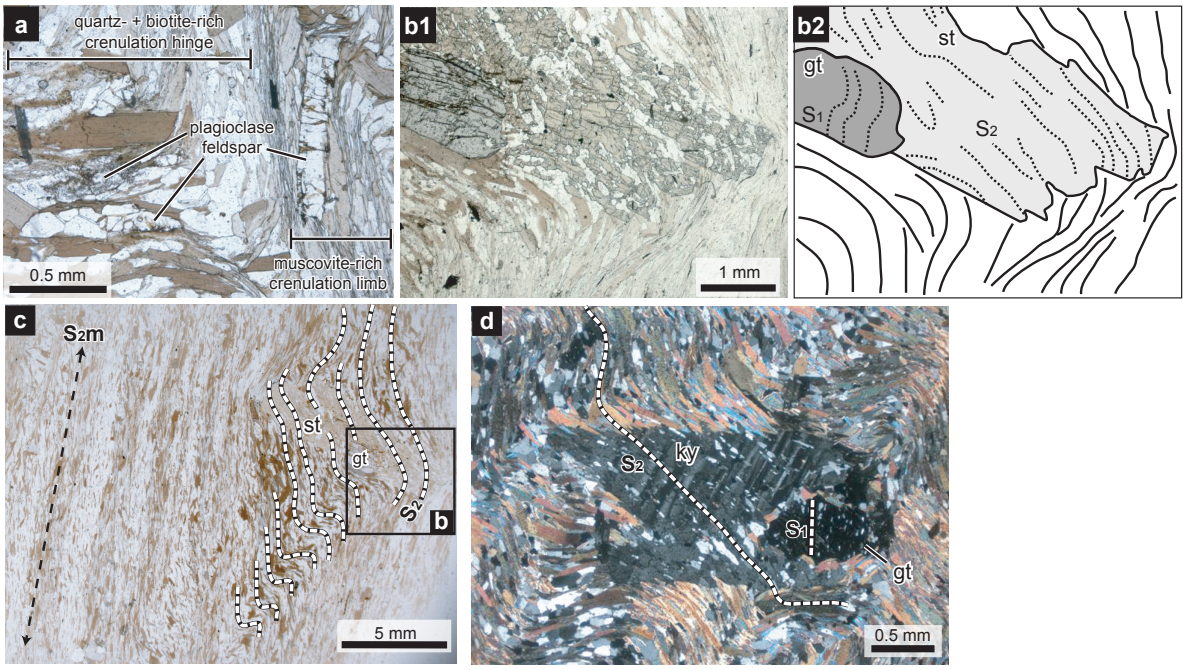

Fig. 4. Microphotographs of pelites from locality 8: (a) Sample 8i. S_1 plagioclase feldspar in S_2 crenulation cleavage is both fractured and altered (fractures rimmed by red-orange alteration product and/or dusty-looking internal alteration). Quartz is clear with low relief; laths of biotite and muscovite are dark and light grey respectively; (b) Sample 8i (b2 is a line-drawing of b1). Syn-tectonic garnet porphyroblast with faintly sinusoidal inclusion trails (S_1 weakly deformed by D_2) occluded by a large staurolite porphyroblast. Staurolite overprints S_2 (quartz inclusion trails oblique to S_1 in garnet), and towards its tip overprints a modified (by D_3) S_2 fabric (also see (c)). D_3 out-lasts staurolite growth and fine laths of S_2 muscovite are wrapped around the tip of staurolite; (c) to show context of (b). S_2 (inclusion trails in staurolite) have been subsequently modified (S_2m) by D_3, tightening the S_2 crenulation cleavage and wrapping large porphyroblasts. Asymmetric pressure shadows suggests a component of simple shear and/or rotation of staurolite during D_3; (d) Sample 8ii. Cross polarised light. A garnet porphyroblast with S_1 inclusion trails is occluded by a kinked kyanite porphyroblast, with S_2 inclusion trails oblique to S_1. Post-kyanite growth, S_2 has been micro-folded against the porphyroblast during D_3.

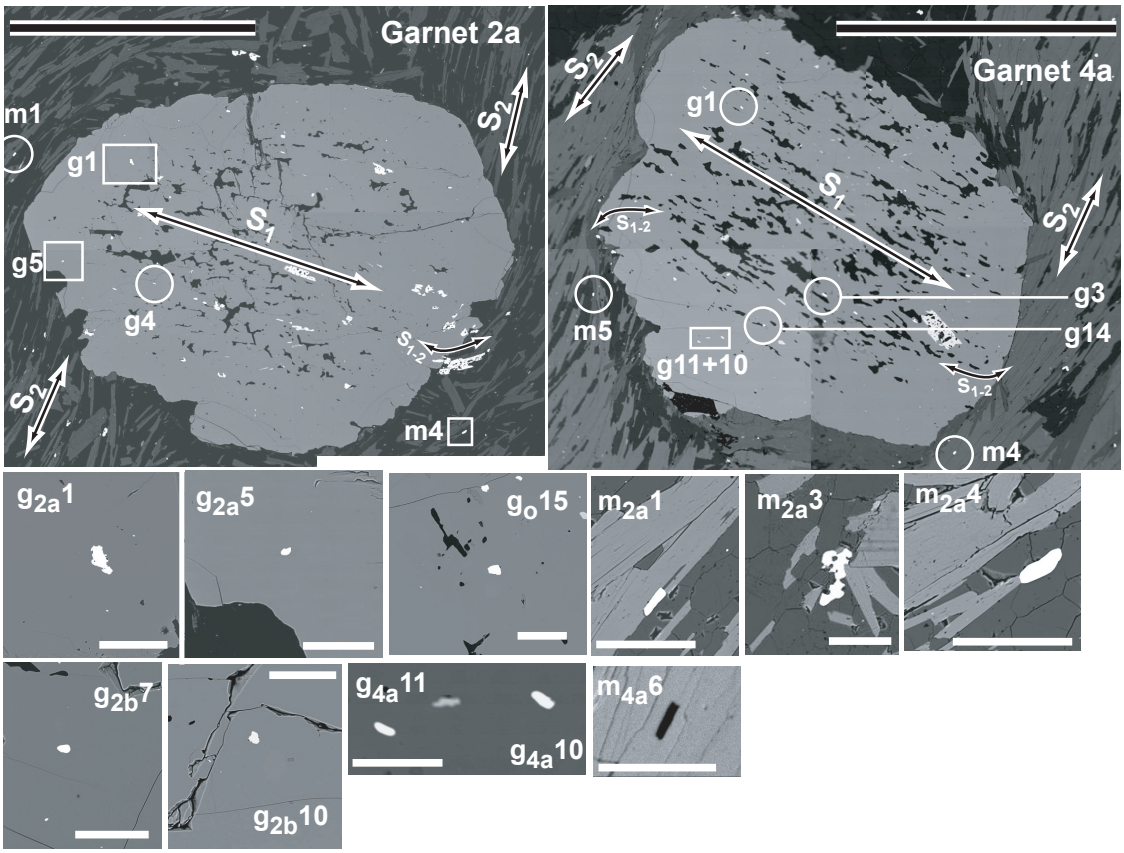

Fig. 5. Back-scatter electron images of two garnet porphyroblasts from sample 14i, plus a selection of the monazite grains analysed (including one Mg-element map, of monazite "$m_{4a}6$"). Garnets overprint a pre-existing S_1 fabric, as well as an S_1–S_2 fabric at the rim consistent with late stage garnet growth syn-tectonic with early D_2. S_2, defined by the biotite/plagioclase matrix (light and dark grey matrix phases respectively), is oblique to S_1 and wraps garnet porphyroblasts. Chlorite (mid-grey between biotite and plagioclase) is present in the pressure shadows to garnet 4a (top and bottom of the image). Monazites are labelled with a prefix 'g' (garnet) or 'm' (matrix) which refers to the host phase, a subscript which refers to the section name (e.g. '2') and the occluding or adjacent garnet (e.g. 'a'), and a suffix which indicates the analysis number (Table 2). Where elongate, monazite grains are aligned with the tectonic fabric (e.g. "$m_{2a}1$", "$m_{4a}6$"). Some other grains are distinctly anhedral (e.g. "$g_{2a}1$" and "$m_{2a}3$"). Black scale bar (garnet images) 2 mm; white scale bar (monazite grain images), 100 μm.

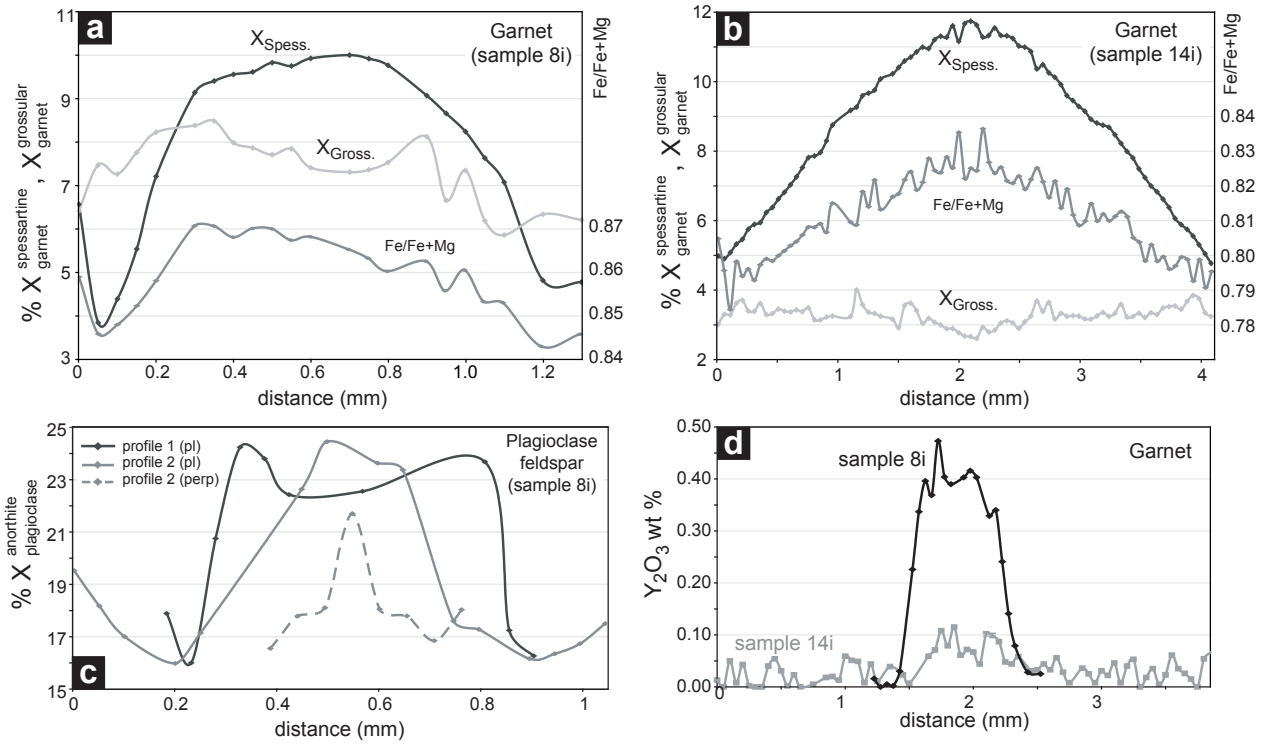

Fig. 6. Chemical zoning in porphyroblasts (data provided in Appendix A): (a) and (b) major element variation across garnets from samples 8i and 14i respectively; (c) anorthite variation across plagioclase feldspars from both samples 8i and 14i, plotted so that their cores are aligned, 'pl' and 'perp' refer to parallel and perpendicular (respectively) to the length of the crystal; (d) Y variation across garnets from both samples 8i and 14i, plotted so that their cores are aligned.

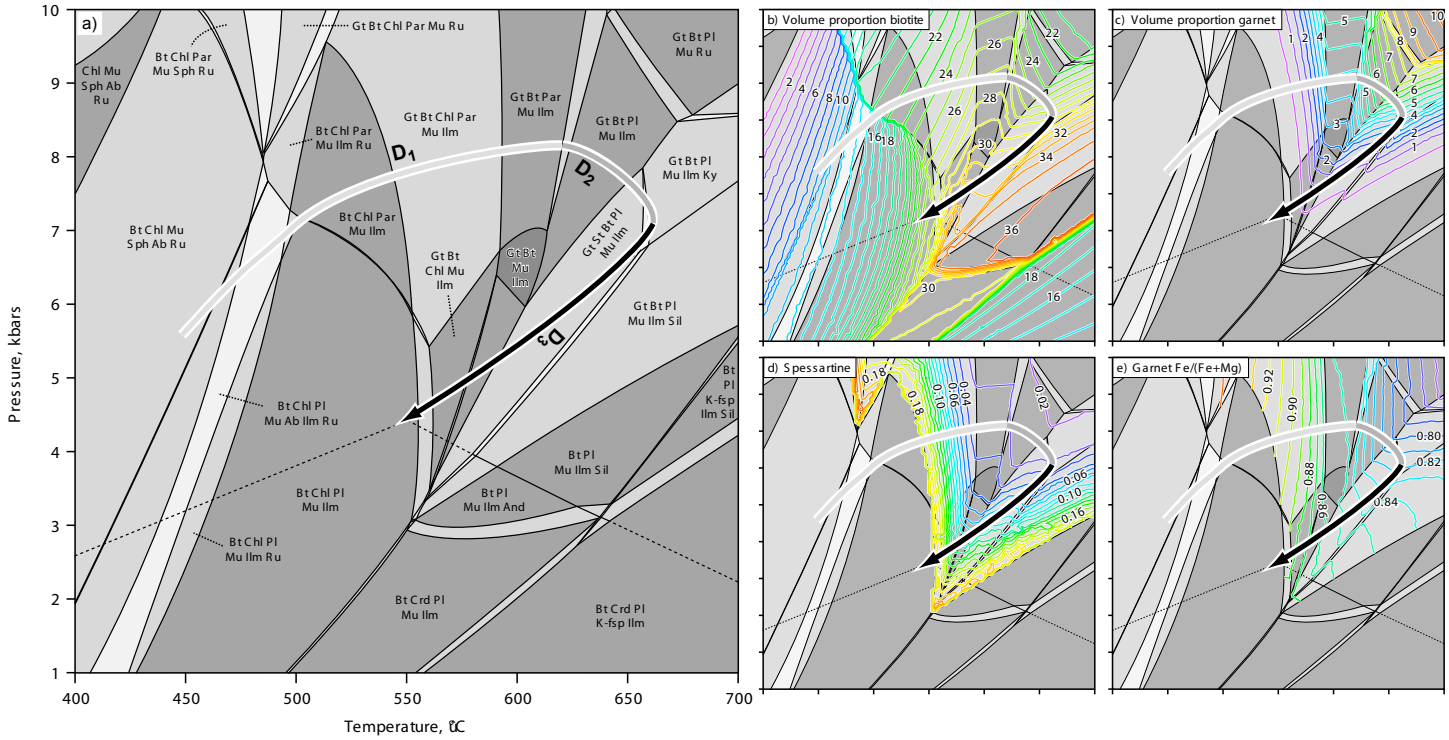

Fig. 7. (a) Pseudosection diagram for sample 8i, quartz and water also stable in every field. Best fit *P–T–d* path (including D_1, D_2 and D_3) shown. Abbreviated phases are garnet (Gt), staurolite (St), biotite (Bt), chlorite (Chl), muscovite (Mu), paragonite (Par), ilmenite (Ilm), rutile (Ru), plagioclase (Pl), titanite (Sph), albite (Ab), kyanite (Ky), sillimanite (Sil), andalusite (And), cordierite (Crd) and K-feldpsar (K-fsp). Al_2SiO_5 phase transitions are shown with solid lines in Al_2SiO_5-bearing fields and are extended into Al_2SiO_5-absent fields with dashed lines. Small assemblage fields unlabelled for clarity. Melt was not considered. Subplots (b) and (c) show calculated abundance of biotite and garnet, respectively. Subplots (d) and (e) show calculated garnet composition, $X_{garnet}^{spessartine}$ and Fe/Fe+Mg ratio, respectively. All subplots are at the same scale (have equivalent axes) to the main plot. Supplementary subplots are provided online.

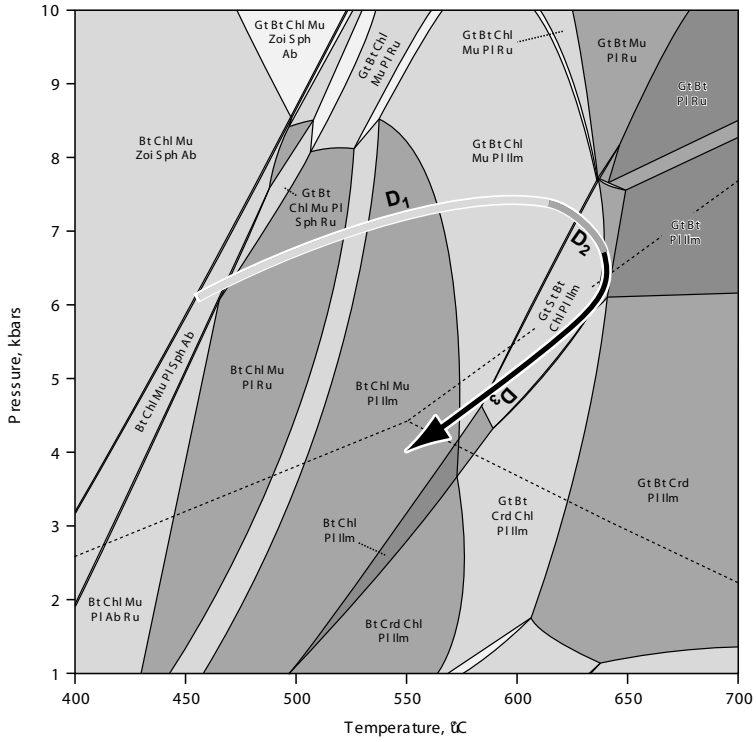

Fig. 8. Pseudosection diagram for sample 14i, quartz and water also stable in every field. Best fit *P–T–d* path (including D_1, D_2 and D_3) shown. Abbreviated phases as in Figure 7 plus zoisite (Zoi). Al_2SiO_5 phase transitions are shown with solid lines in Al_2SiO_5-bearing fields and are extended into Al_2SiO_5-absent fields with dashed lines. Small assemblage fields unlabelled for clarity. Melt was not considered. Supplementary subplots are provided online.

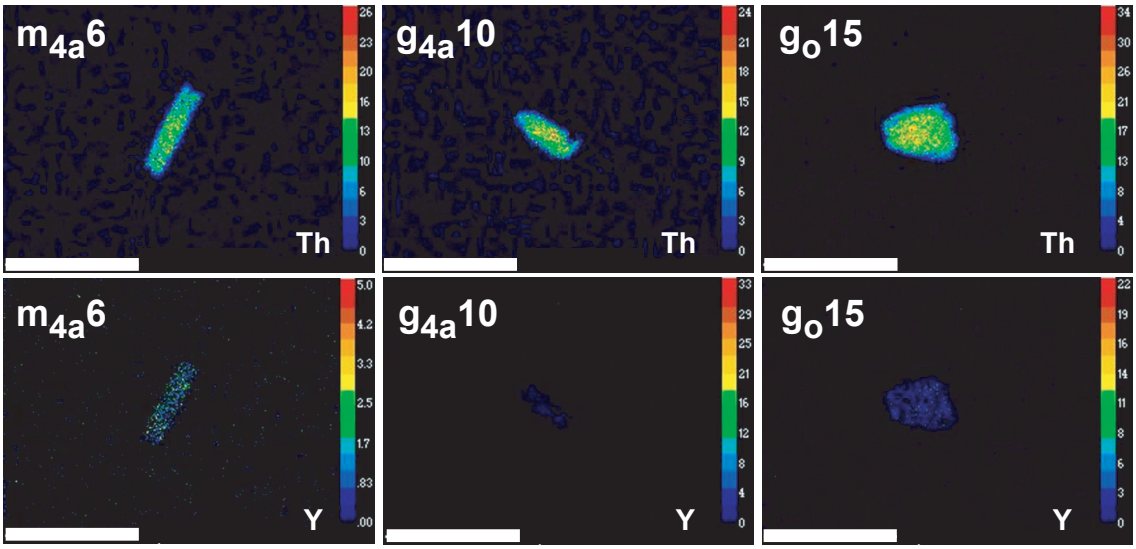

Fig. 9. Th and Y maps of three representative monazite grains in sample 14i. Grains are normally zoned with respect to Th, whereas the concentration of Y is extremely low or beyond the levels of detection. See figure 5 for corresponding BSE images. Scale bar 50 µm.

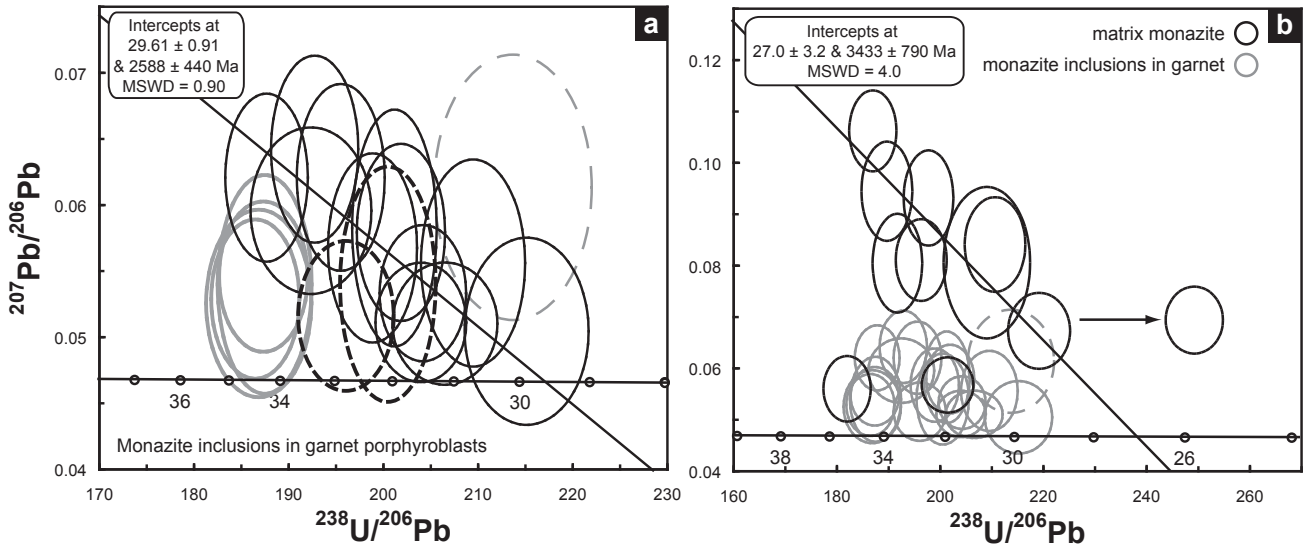

Fig. 10. U–Pb monazite data from sample 14i. (a) Monazite inclusions in garnet porphyroblasts: black ellipses used in regression to a c. 30 Ma U–Pb age; bold grey ellipses (of inclusions in the same garnet crystal) indicate a U–Pb age of c. 34 Ma; dashed black ellipses are inferred to represent c. 34 Ma monazites with a component of Pb loss; dashed grey ellipse omitted from regression owing to relatively large errors. (b) All data: grey ellipses represent all analyses shown in a); the regression is through all analyses of matrix monazite grains bar 3. See text for more details. Data point error ellipses are 2s .

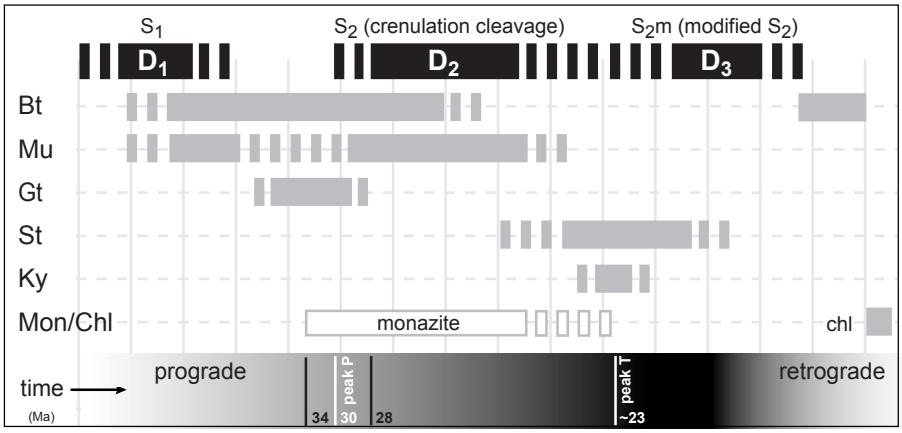

Fig. 11. Summary of the relative timing of metamorphism and deformation recorded in the Haimanta Group. Abbreviated mineral phases as in Figure 7.

Appendix

Representative electron-microprobe analyses (EPMA) of zoned major minerals in samples 8i and 14i (Haimanta Group pelites) (Fig. 6)

	Weight % oxide									Cations per formula unit								% End-members	
Garnet	SiO_2	TiO_2	Al_2O_3	FeO	MnO	MgO	CaO	Y_2O_3	Total	Si	Al	Fe^{3+}	Fe^{2+}	Mn	Mg	Ca	Fe/(Fe+Mg)	Spess.	Gross.
8i																			
core	37.13	0.01	21.10	32.14	4.40	2.77	2.57	0.40	100.53	2.99	2.00	0.03	2.13	0.30	0.33	0.22	0.87	10.03	7.32
inner rim	37.74	0.00	21.65	34.17	1.71	3.46	2.67	0.00	101.40	2.98	2.02	0.02	2.23	0.11	0.41	0.23	0.85	3.83	7.49
inner rim	37.88	0.00	21.55	34.31	2.15	3.55	2.28	0.03	101.75	2.99	2.00	0.03	2.23	0.14	0.42	0.19	0.84	4.81	6.34
14i																			
core	37.52	0.04	21.31	32.51	5.11	3.82	1.02	0.06	101.37	2.97	1.99	0.06	2.10	0.34	0.45	0.09	0.82	11.52	2.82
rim	38.16	0.03	21.63	33.80	2.20	4.82	1.19	0.03	101.84	2.99	1.99	0.03	2.18	0.15	0.56	0.10	0.80	4.87	3.27
rim	38.18	0.01	21.52	33.83	2.14	4.83	1.16	0.05	101.73	2.99	1.99	0.03	2.19	0.14	0.56	0.10	0.79	4.74	3.21

Plagioclase	SiO_2	Al_2O_3	FeO	Na_2O	K_2O	CaO	Total	Si	Al	K	Na	Ca	% Anorthite
8i - profile 1 (parallel)													
inner core	62.13	23.04	0.09	8.51	0.06	4.47	98.31	2.79	1.22	0.00	0.74	0.22	22.43
outer core	62.35	23.59	0.08	8.44	0.07	4.92	99.44	2.77	1.24	0.00	0.73	0.23	24.25
outer core	60.17	22.84	0.04	8.07	0.05	4.55	95.72	2.77	1.24	0.00	0.72	0.22	23.69
inner rim	64.62	22.49	0.12	9.40	0.08	3.25	99.95	2.84	1.17	0.00	0.80	0.15	15.97
rim	64.47	22.63	0.06	9.29	0.12	3.29	99.86	2.84	1.18	0.01	0.79	0.16	16.24
rim	63.89	22.63	0.20	9.15	0.08	3.62	99.56	2.83	1.18	0.00	0.79	0.17	17.87
8i - profile 1 (parallel)													
inner core	62.41	23.84	0.03	8.47	0.05	4.98	99.78	2.77	1.24	0.00	0.73	0.24	24.46
outer core	62.76	23.58	0.02	8.63	0.09	4.61	99.69	2.78	1.23	0.01	0.74	0.22	22.64
outer core	62.42	23.47	0.06	8.62	0.07	4.78	99.42	2.78	1.23	0.00	0.74	0.23	23.38
inner rim	64.41	22.39	0.03	9.42	0.08	3.25	99.58	2.85	1.17	0.00	0.81	0.15	15.96
inner rim	64.42	22.32	0.03	9.38	0.07	3.28	99.51	2.85	1.16	0.00	0.80	0.16	16.14
rim	63.57	23.08	0.07	9.09	0.07	4.01	99.89	2.81	1.20	0.00	0.78	0.19	19.52
rim	63.77	22.56	0.08	9.24	0.07	3.56	99.29	2.83	1.18	0.00	0.79	0.17	17.49
8i - profile 1 (perp.)													
core	61.93	22.58	0.03	8.51	0.08	4.30	97.43	2.80	1.20	0.00	0.75	0.21	21.70
inner rim	64.60	22.27	0.05	9.29	0.08	3.42	99.71	2.85	1.16	0.00	0.79	0.16	16.83
rim	64.23	22.38	0.02	9.24	0.10	3.34	99.30	2.84	1.17	0.01	0.79	0.16	16.53
rim	64.45	22.77	0.09	9.35	0.07	3.74	100.46	2.83	1.18	0.00	0.80	0.18	18.01
14i													
core	65.23	21.84	0.06	9.68	0.06	2.86	99.73	2.87	1.13	0.00	0.83	0.13	13.97
core	65.19	21.94	0.05	9.73	0.07	2.83	99.80	2.87	1.14	0.00	0.83	0.13	13.78
rim	64.57	22.54	0.09	9.35	0.07	3.39	100.01	2.84	1.17	0.00	0.80	0.16	16.63
rim	64.61	22.38	0.10	9.43	0.08	3.38	99.98	2.84	1.16	0.00	0.81	0.16	16.46

Sample 8i, supplementary subplots to Fig. 7 (Chambers et al.)

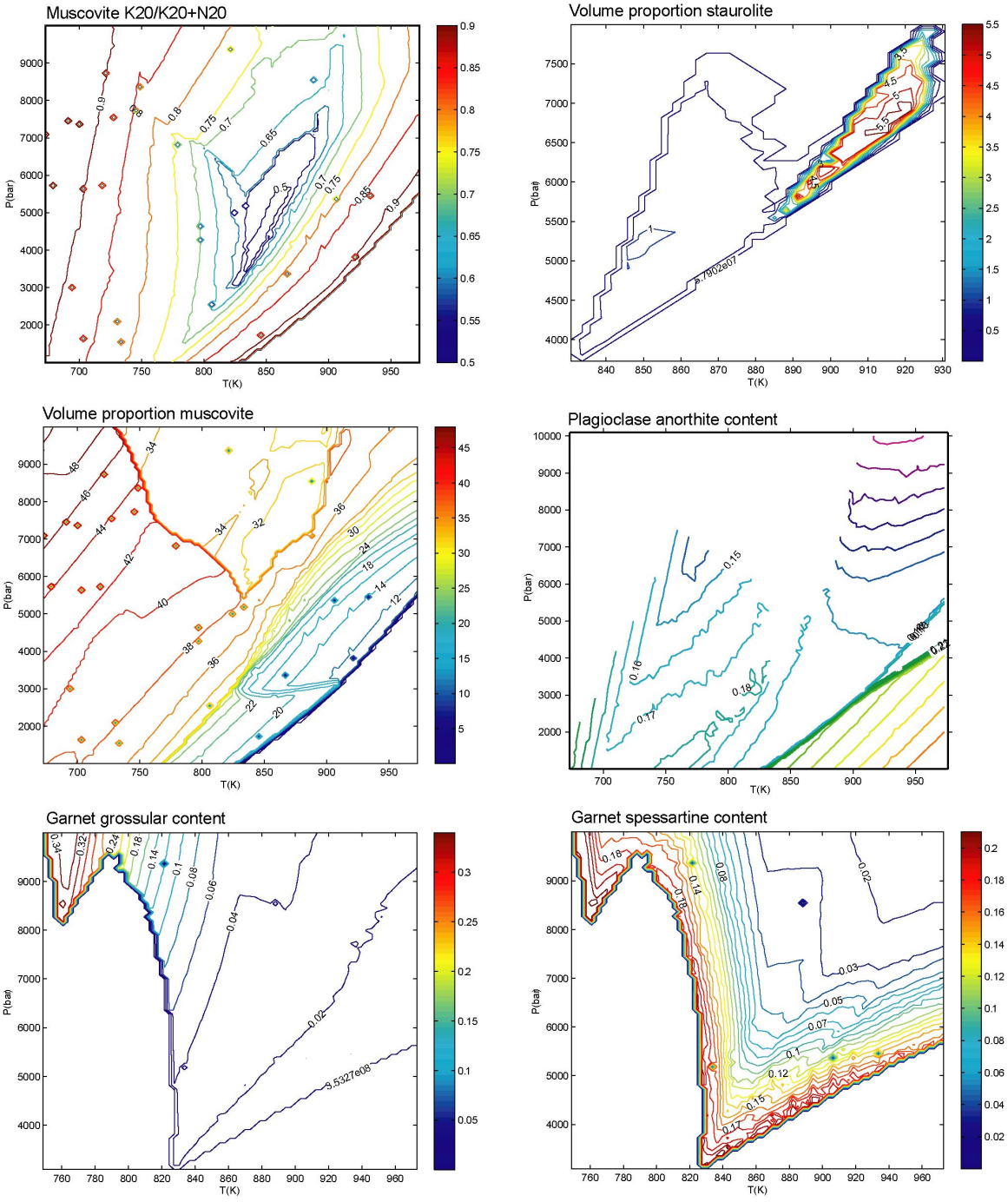

Sample 14i, supplementary subplots to Fig. 8 (Chambers et al.)

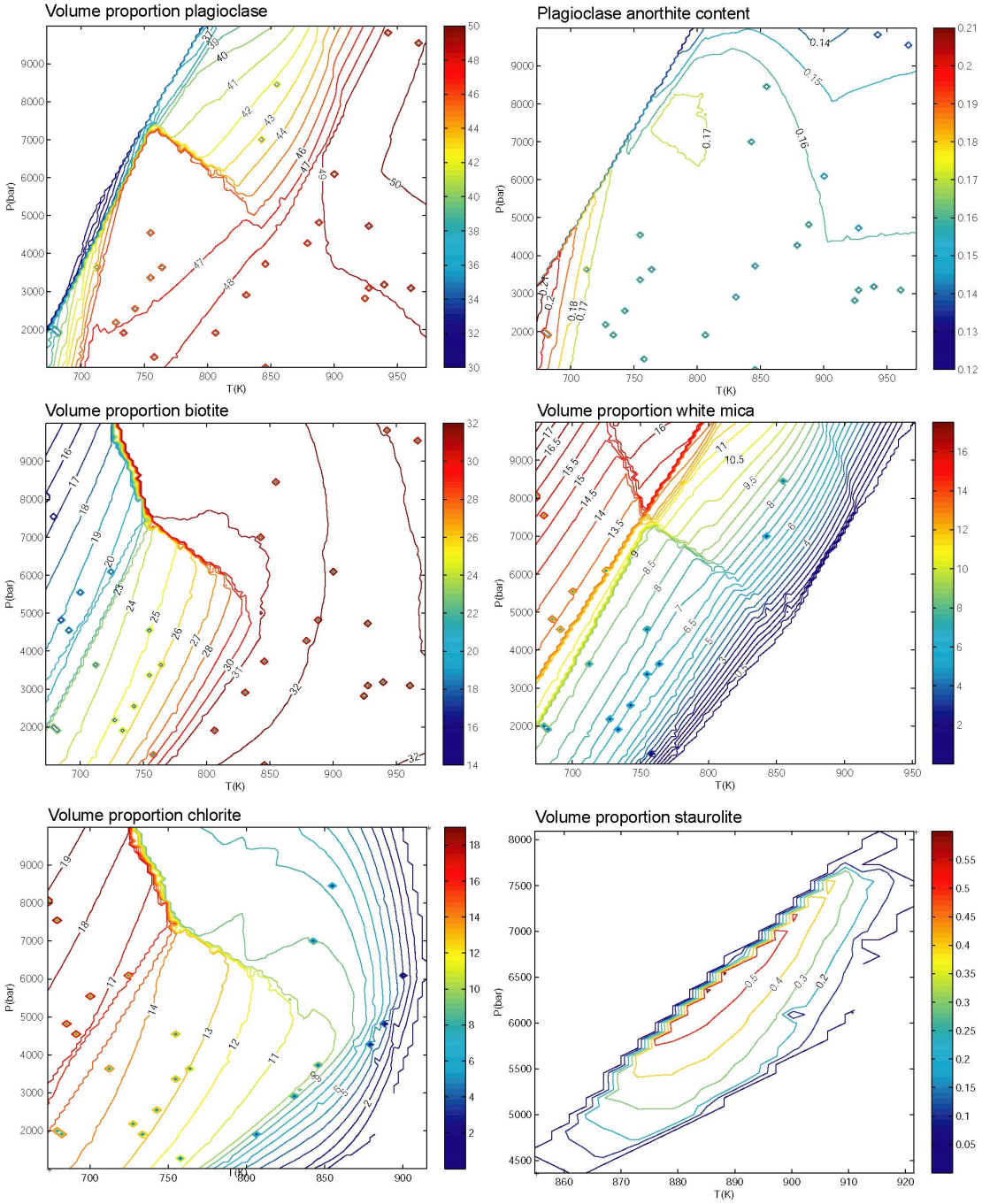

Sample 14i, supplementary subplots to Fig. 8 (Chambers et al.) cont.